in prep.

From Radio to X-ray: The Quiescent Atmosphere of the dMe Flare Star EV Lacertae

Rachel A. Osten[1]

Astronomy Department, University of Maryland, College Park, MD 20742-2421; rosten@astro.umd.edu

Suzanne L. Hawley

Astronomy Department, Box 351580, University of Washington, Seattle, WA 98195; slh@astro.washington.edu

Joel Allred

Physics Department, Box 351560, University of Washington, Seattle, WA 98195; jallred@u.washington.edu

Christopher M. Johns-Krull

Physics & Astronomy Department, Rice University, 6100 Main Street, Houston, TX 77005; cmj@rice.edu

Alexander Brown, Graham M. Harper

Center for Astrophysics and Space Astronomy, University of Colorado, 593 UCB, Boulder, CO 80309-0593; ab@casa.colorado.edu,gmh@casa.colorado.edu

ABSTRACT

We report on multi-wavelength observations spanning radio to X-ray wavelengths of the M dwarf flare star, EV Lacertae, probing the characteristics of the outer atmospheric plasma from the upper chromosphere to the corona. We detect the star at a wavelength of 2 cm (15 GHz) for the first time. UV and FUV line profiles show evidence of nonthermal broadening, and the velocity width appear to peak at lower temperatures than in the Sun; this trend is confirmed

---

[1] Hubble Fellow

in another active M dwarf flare star. Electron density measurements indicate nearly constant electron pressures between $\log T$ =5.2 and 6.4. At higher coronal temperatures, there is a sharp increase of two orders of magnitude in density ($n_e \sim 10^{13}$ cm^{-3} at $\log T$ =6.9). X-ray, EUV, FUV and NUV spectra constrain the DEM from the upper chromosphere through the corona. The coronal pressures are inconsistent with the assumption of hydrostatic equilibrium, either through EM modeling or application of scaling laws, and imply large conductive loss rates and a large energy input at the highest temperatures. The timescales for radiative and conductive losses in EV Lac's upper atmosphere imply that significant continued heating must occur for the corona to maintain its quiescent properties. The high frequency radio detection requires the high temperature X-ray-emitting coronal plasma to be spatially distinct from the radio emission source. Length scales in the low-temperature corona are markedly larger than those in the high-temperature corona, further suggestions of an inhomogeneous mixture of thermal and nonthermal coronal plasma.

Subject headings: stars: activity, stars: coronae, stars: late-type, radio continuum: stars, X-rays: stars, ultraviolet: stars

1. Introduction

By studying the properties of extreme coronae, such as on M dwarf flare stars, clues to common physical processes arising on these stars and our low-activity Sun can be investigated. dMe stars are small, and have intense magnetic fields covering a large majority of the stellar disk (Johns-Krull & Valenti 1996; Saar 1994). The transition to fully convective stars occurs at spectral type close to M4V, so dMe stars with spectral types earlier than this are close to being fully convective. Despite their small size, dMe flare stars produce significant coronal emission, in many cases near the maximum ($L_x/L_{bol} \sim 10^{-3}$) that any star is able to maintain in the quiescent state (Vilhu & Walter 1987; Hempelmann et al. 1995). How different are coronal structures on dMe stars compared to the Sun, and other active stars? The large magnetic filling factors inferred for the photospheres of dMe stars suggest a stark contrast with the Sun's small (<1%) sunspot area coverage. Recent results from X-ray spectra have indicated that the elemental fractionation pattern seen in most active stars, including active M dwarfs, is opposite that seen on the Sun. In the solar corona lines with First Ionization Potential (FIP) <10 eV are enhanced relative to those with greater FIP; this is referred to as the First Ionization Potential (FIP) effect. At temperatures less than about 1 MK, the FIP effect disappears from full-disk observations of the Sun (Laming et al. 1995), and lower-temperature structures do not show the FIP effect. In active stellar coronae, elements with FIP >10 eV appear enhanced relative to those with lower FIP. The properties of time-averaged active stellar coronae appear to resemble solar flares, with elevated temperatures and densities.

The n_e^2 dependence of the emissivity in transitions appearing in the UV through X-ray skews analysis to the densest structures, but still allows an investigation of gross coronal properties. As Rosner et al. (1978) remarked, "spatially unresolved observations of stellar coronae represent a statistical smoothing of widely disparate plasma structures." Reconstructions of the emission measure distribution of plasma, and the dependence of electron density, with temperature, $n_e(T_e)$, from high spectral resolution grating data give constraints on stellar coronal structure and heating. Another motivation for a detailed investigation of the outer atmosphere of an M dwarf flare star lies in recent studies which suggest that the occurrence of flares may be frequent enough to supply the heating requirements of some stellar coronae (Güdel et al. 2003, but first put forth in Parker (1988)). Recent studies on the Sun are still inconclusive about the role of micro- and nano-flares in providing the steady X-ray luminosity (Krucker & Hudson 2004). If flares are the dominant source providing coronal heating in dMe flare stars, then the atmospheric properties should reflect that.

EV Lac (Gliese 873) is a young disk population dM3.5e star at a distance of 5 pc. It is the second brightest M dwarf X-ray source seen in the ROSAT All-Sky Survey, with a quiescent 0.1–2.4 keV flux of $\sim 4\times 10^{-11}$ erg cm^{-2} s^{-1} (Hünsch et al. 1999). The quiescent X-ray luminosity is a significant fraction of the total bolometric luminosity ($\sim$0.2%), near the maximum of any star in its quiescent (non-flaring) state. Its low mass (0.3 $M_\odot$; Delfosse et al. 1998) puts it near the dividing line for fully convective stars. EV Lac has very strong, 4 kG magnetic fields covering $>$ 50% of the stellar surface (Johns-Krull & Valenti 1996; Saar 1994) so coronal phenomena are dominated by the interactions of these close-packed magnetic field lines. Recent investigations of the H Lyman-α profile have determined the existence of a stellar wind through detection of an astrosphere (Wood et al. 2005b), with an estimated mass loss rate very similar to the solar mass loss rate (Wood et al. 2005a).

Based on its previous record for large and dramatic flare variability, we studied the multi-wavelength behavior of EV Lac with observations utilizing the *Chandra X-ray Observatory*, the *Hubble Space Telescope*, ground-based optical photometry and spectroscopy, and ground-based radio interferometry, over a period of two days in September 2001. Many flares were detected; a separate paper (Osten et al. 2005) discusses the flare observations. The focus of this paper is an investigation of EV Lac's quiescent atmospheric properties from X-ray to radio wavelengths.

2. Observations and Data Reduction

2.1. VLA

EV Lac was observed with the NRAO[1] Very Large Array on 19 and 20 September 2001. The array was moving from C to D configuration. The phase calibrator was 2255+420, and the flux density calibrator was 0137+331 (3C 48). The observations on 19 September 2001 were performed using the entire array, and frequency switched between 6, 3.6, and 2 cm (4.9, 8.4, and 15.0 GHz), for a total of 10 hours of observations. On 20 September, the observing strategy changed: we observed simultaneously in two subarrays at 6 and 3.6 cm, to characterize the dual frequency behavior of any flares that might occur during the Chandra observations. Processing of the data was done in AIPS (version 31 Dec 03). The field around EV Lac is crowded; there is a large radio galaxy $\sim$ 2.7 arcminutes away, and numerous radio sources. We performed multi-field cleaning, taking advantage of the NVSS radio survey to locate possible bright radio sources in the primary beam and sidelobes. After imaging the field, visibilities of sources not identified as EV Lac were removed, and the field was re-imaged. The quantities measured are the total flux, I, the amount of circularly polarized flux, V, and the percentage of circular polarization, π_c is defined as

$$\pi_c(\%) = \frac{V}{I} \times 100 \quad . \tag{1}$$

2.2. HST

EV Lac was observed with the *HST-STIS* for 4 orbits on 20 September 2001. The data were obtained in the Cycle 9 program 8880 with the E140M grating, centered at 1425 Å using the FUV-MAMA detector and the 0.2x0.2 arcsec aperture. The wavelength range covered was 1140–1735 Å in 44 orders, with an approximate resolving power of $R = 45,000$. The data were acquired in TIME-TAG mode to enable investigation of short time-scale variability at high spectral resolution.

Spectra were extracted in 60 second intervals to search for significant variability; the order location solutions from the pipeline-processed data were used to extract spectra and assign wavelengths. The background and spectral extraction widths were 7 pixels, and the background was fit by a second order polynomial; the background was then subtracted to

---

[1] The National Radio Astronomy Observatory is a facility of the National Science Foundation operated under cooperative agreement by Associated Universities, Inc.

obtain a net spectrum. We constructed a light curve by summing the background-subtracted counts in each 60 second spectrum, using Poisson statistics to generate error bars. A quiescent spectrum was constructed by excluding times of flaring activity. The net quiescent exposure time was 10,320 seconds (total exposure 10,920 s).

2.3. FUSE

EV Lac was observed with the *Far Ultraviolet Spectroscopic Explorer (FUSE)*[2] in the Cycle 3 program C1140201 (PI A. Brown) on 1 July 2002. An overview of the *FUSE* mission and the on-orbit performance are described in Moos et al. (2000) and Sahnow et al. (2000), respectively.

The data for EV Lac were collected in time-tagged mode through the 30×30 arcsec LWRS apertures chosen to maximize the data collected in the SiC channels (920 – 1100Å) which can be lost from smaller apertures owing to thermal misalignment of the telescope. Our subsequent examination of the stellar signal suggests that the target were within the apertures throughout the observation. The spectral resolution using the LWRS is typically $R \sim 15,000$ ($20\,\mathrm{km\,s^{-1}}$). The raw spectra were calibrated with CalFUSE v2.4.0 (Kruk et al. 2001); the location of the extraction windows were manually selected and optimally aligned, with the orbital day and night spectra being extracted separately. The 38 ks observation contained approximately 16 ks and 20 ks of orbital day and night, respectively. We adopted the default burst screening parameters and background subtraction.

2.4. EUVE

We make use of an earlier observation of EV Lac with the Extreme Ultraviolet Explorer (EUVE), in order to fill in critical temperature regions. EV Lac was observed by EUVE in 1993, from 9–17 September. For more information on the EUVE mission and instruments see Bowyer & Malina (1991). Processing of the data used specialized reduction procedures in IRAF and IDL[3] (see Osten et al. 2003); briefly, times of large background were excluded,

---

[2] Based on observations made with the NASA-CNES-CSA Far Ultraviolet Spectroscopic Explorer. *FUSE* is operated for NASA by the Johns-Hopkins University under NASA contract NAS5-32985.

[3] IRAF is distributed by the National Optical Astronomy Observatories, which is operated by the Association of Universities for Research in Astronomy, Inc., under contract to the National Science Foundation (USA).

and events falling within a circular region around the source were tagged for source spectral extraction; an annular region around the source region was tagged as background. A light curve was generated by binning source and background photons and subtracting the background. Times of obvious flaring were excluded. A net spectrum was extracted for the short wavelength (SW) and medium wavelength (MW) spectrometers, respectively. The net exposure time was 105ks for each spectrometer.

Inspection of the MW spectrum revealed the presence of two transitions of Fe XVI, at λ 335.41 and λ 360.76, whose ratio can be used to constrain the column density of intervening interstellar hydrogen. Previous high energy missions (e.g., Sciortino et al. 1999) have used N_H of 10^{19} cm^{-2}; the ratio of the two Fe XVI lines gives $N_H \sim 4{\times}10^{18}$ cm^{-2} based on interstellar cross sections in Morrison & McCammon (1983) and the contribution functions tabulated in Brickhouse et al. (1995). We adopt this value for correction of observed EUV and X-ray emission lines.

2.5. Chandra Observations

The primary focus of the investigation was a unique 100 ks Chandra observation, from 2001 September 19.8–21.0. The observations were made using the High Energy Transmission Grating Spectrometer (HETGS) in conjunction with the ACIS-S detector array[4]. The HETGS provides an undispersed image of the object from 0.3–10 keV and spectra through two gratings: the Medium-Energy Grating (MEG) covering the wavelength range 1.7–31 Å in first order and the High Energy Grating (HEG) covering the wavelength range 1.2–18.5 Å in first order, with almost twice the spectral resolution. Processing the Chandra data utilized CIAO, Version 2.2, "threads", i.e., processing recipes, for different aspects of the data reduction. We eliminated bad aspect times and confirmed that the observation was not affected by ACIS "background flares". The new ACIS pixel size (0.0239870 mm) and focal length (10070.0 mm) were updated in processing the ACIS events. Events with energies less than 300 eV and greater than 10,000 eV were excluded, as these are not well-calibrated; also excluded were events whose pulse-height invariant (PI) values were 0,1, or 1024 (overflow/underflow values). Only ASCA grades 0,2,3,4,6 were kept. The events were resolved into spectral events using region filtering (rectangles around the MEG and HEG stripes), and a level 2 event file was generated. One of the CCD chips in the ACIS-S array (S4) suffered increased scatter (streaking) in the horizontal (CHIPY) direction, apparently caused by a

---

[4] More information about Chandra and its instruments can be found at http://cxc.harvard.edu/proposer/POG/html/MPOG.html

flaw in the serial readout; a destreak filter was applied to remove these data. Updated sensitivity files were used to correct for contamination on the ACIS chip which affects sensitivity at low energies.

We used custom IDL procedures to determine light curve variations and subsequent spectral analysis. The level 2 events file was filtered for MEG events falling within the spectral extraction window (±0.1 mm in the cross-diffraction coordinate). The first ∼40 ks of the observation were unaffected by flares; the remaining 60 ks was characterized by numerous small enhancement events and a few high contrast, but short duration, events. A separate paper details the X-ray flare variations in context of the multi-wavelength nature of the monitoring campaign (Osten et al. 2005). Little difference is apparent in the spectra of time intervals affected by small flares and those characterized by quiescence, so we extracted spectra corresponding to the sum of the initial quiescent period and a later interval marked by small enhancements (flares 3–6 and 9 in the terminology of Osten et al. 2005) for this study. The total exposure time of the extracted interval is 65 ks.

3. Analysis

3.1. Radio

The flare campaign described by Osten et al. (2005) focused on the large flare observed at 3.6 and 6 cm on 20 September 2001. Here we concentrate on the 19 September and quiescent part of the 20 September radio observations. Flux and polarization parameters for the data on 19 September are listed in Table 1; values for 20 September are listed in Osten et al. (2005). Figure 1 plots the flux and polarization spectra. In addition to determining the average flux density of the source at three frequencies on 19 September, we investigated the temporal variations to ensure that no large flare events occurred. We detect the source at 2 cm for the first time. The spectral index between 6 and 3.6 cm (assuming $S_\nu \propto \nu^\alpha$) is -0.16 ± 0.11 (1σ), while between 3.6 and 2 cm it is -0.55 ± 0.18 ($1\ \sigma$). The 6 and 3.6 cm circular polarization values are almost the same as the “preflare” values recorded on 20 September, and reported in Osten et al. (2005), and the 3.6 cm fluxes are very similar as well. The largest variation is in the 6 cm flux on 19 and 20 September, but it is less than 30%. Thus we have confidence that the quiescent conditions in the radio-emitting corona were at a characteristic level during all the observations described here.

3.2. Line Fluxes

3.2.1. HST

The quiescent STIS spectrum, characterized by bright emission lines, is shown in Figure 2. We fit moderate and strong emission lines using a Gaussian line profile analysis, convolving the line profile fit with the empirical line spread function to account for instrumental broadening appropriate for the aperture and grating. [5] We use the laboratory wavelengths in the stellar rest frame, corrected for EV Lac's radial velocity of -1.5 km s^{-1} (Duflot et al. 1995). Table 2 lists the derived velocities, widths, and fluxes.

In the case of O V λ1218, we fitted the wing of H Lyα as a second order polynomial to subtract and fit the O V line. The transition of Fe XXIV λ1354 is blended with a C I transition, and requires careful modeling of the expected flux from the C I line to remove its influence on the Fe XXIV profile. We used the line flux listed in Ayres et al. (2003), who included EV Lac in their survey. The contaminating influence of the C I transition is weak in this case, as estimates from simple Gaussian fitting to the line profile are similar to those obtained from the more sophisticated approach. We fit the C III multiplet from 1174.9–1176.4 Å as the sum of six Gaussians, with central wavelengths fixed to the laboratory values, and FWHM and amplitudes allowed to vary.

We also checked that line ratios of transitions selected for use in emission measure analysis were consistent with the effectively thin flux ratios. Table 3 lists the transitions, the expected effectively thin ratios, as well as the observed values. The observed ratio of Si II λ1533.430/λ1526.706 is slightly lower than the effectively thin ratio, as is C III λ1175.713/λ1174.935. This is consistent with trends reported in the Sun and other stars (Del Zanna et al. 2002, and references therein). The C III transitions share a common upper level so their ratio will depart from the optically thin values when there is opacity in the line — the deviation is that expected from line scattering in these systems. They can still be considered effectively thin if no photons are destroyed. The magnitude of the departures is small, and we use the total line fluxes to estimate the DEM at these temperatures (see §5.2). For line profiles which were fit better by the sum of two Gaussian line profiles, we compared the flux ratios of the narrow and broad components separately. For the Si IV and C IV doublets, the flux ratio of each narrow component, as well as the flux ratio of each broad component, is consistent within the errors with the effectively thin flux ratio.

---

[5] Tabulated line spread function data is available from http://www.stsci.edu/hst/stis/performance/spectral_resolution

3.2.2. FUSE

The data were split into night-time and day-time data so that the effects of air-glow emission are recognizable. No obvious flaring was detected during the observation. The spectra containing the detected transition region emission lines are shown in Figure 3. The only stellar lines detected are O VI $\lambda\lambda$1031.9,1037.6, the C III λ1175 multiplet and the λ 977 resonance line, and the forbidden transition Fe XVIII λ974. A comparison of the day-time and night-time spectra show that the O VI lines and the C III intersystem multiplet are unaffected by airglow features. The day-time data for the C III 977 Å profile show the presence of significant scattered solar C III photons in the SiC channels, which is not present during orbital night. Since EV Lac is so near ($d = 5$pc), FUV reddening is likely to be small. Emission line fluxes for these lines were measured by direct summation over the line profiles. No continuum signal was detected in the region of these lines. Line fluxes of detected lines are listed in Table 4.

3.2.3. EUVE and Chandra

The EUV and X-ray spectra are dominated by lines of highly ionized iron, as well as bright lines arising from transitions of H- and He-like ions in the X-ray region (Figures 4 and 5). These lines are well described as effectively thin transitions occurring in collisional ionization equilibrium. At the spectral resolution of the Chandra HETGS, the lines are unresolved; in our analysis of the line profiles we assume a Gaussian line profile shape with width fixed to the instrumental resolution (23 mÅ for MEG, 11 mÅ for HEG), and we solve for line flux and central wavelength. We generated a list of moderate to strong transitions in the HETG bandpass from the atomic linelists of the APEC (Smith et al. 2001) project to use for line fitting. Widths of EUVE spectral line fits were kept fixed to the instrumental resolution: 0.38 Å for SW, 1.14 Å for MW.

Continuum processes, consisting of free-free, free-bound, and two-photon processes from several elements (but dominated by H and He), can be non-negligible at high energies. As the continuum emission can be important in the EUV spectral region, but difficult to disentangle from the numerous weak lines, we determined the expected amount of continuum emission in the EUV spectral range using the scaling at X-ray wavelengths $\lambda \geq 10$ Å and subtracted this from the observed EUV spectra to estimate continuum-free emission line fluxes. As discussed in §4 in more detail, we utilized a self-consistent treatment of line and continuum emission in order to make a first estimate of the DEM and abundances, and determine EUV/X-ray line fluxes without contribution from continuum emission for further analysis. Line fluxes of detected EUV lines are listed in Table 5. Table 6 lists the detected X-ray transitions used in the DEM, abundance, and electron density analyses described in the next sections, along with the continuum-free estimate of line fluxes.

3.2.4. Variability

Only the STIS and Chandra spectra are strictly simultaneous; the EUVE observation was made ∼8 years earlier, the FUSE observation ∼10 months later. In light of the dramatic variability of dMe stars, it is worthwhile to check whether the state of the star is roughly the same in these three different pointings. We have made some initial cuts to exclude large flares, but smaller levels of variability may exist, and we address that here.

The C III multiplet at λ1175 is present in both STIS and FUSE spectra, taken ∼10 months apart. The line fluxes in the FUSE spectrum are ≈1.6 times larger than the STIS line fluxes. The ionization fraction of the ion C III is a maximum at a temperature ≈ 9×10^4 K. There is evidence for a small amount of variability in the upper chromospheric and transition region plasma. If the DEM has changed slightly between these times, we could expect a difference of this magnitude.

There are coronal transitions in the UV, FUV, EUV, and X-ray whose observed fluxes can be compared against the emissivity ratios for the transitions, to quantify the level of variability at these different times. In the STIS spectral range there is Fe XXI λ1354, and Fe XXI λ128.73 is detected by EUVE. In the FUSE spectral range there is Fe XVIII λ974, and Fe XVIIIλ93.92 is detected by EUVE. The observed fluxes of these lines are compared against the brightest transitions of Fe XVIII and Fe XXI detected in the Chandra bandpass, to determine whether and how much EV Lac varied between the observations. We use $\lambda\lambda$9.48,12.284 as the brightest transitions of Fe XXI, and $\lambda\lambda$14.208,16.07 of Fe XVIII. The emissivity ratios of these transitions have a range, due to their temperature dependence. Since the observed flux is proportional to the emissivity times the DEM, and it is possible that the DEM has changed if the system is variable, we examine a range of emissivity ratios to gauge the extent of variability. By assuming that lines are formed over $\Delta \log T$ =0.3, we calculate the range of emissivities expected. Table 8 lists the observed flux (energy) ratios, along with the emissivity (energy) ratios, over a temperature range of ±0.15 dex from $T_{\rm max}$, the temperature at which the ionization fraction peaks. The observed flux ratios are consistent within the observational errors to the range expected from temperature variations within $\Delta \log T$ =0.3.

Based on the chromospheric and coronal line flux comparisons, we hereby assume that by analyzing these spectra as a whole we are diagnosing a characteristic state of EV Lac.

3.3. Line Profiles

Only the STIS and FUSE spectra have sufficient spectral resolution to perform line profile analysis. Earlier work on active stars by Linsky & Wood (1994) showed that UV emission lines are often better described as the sum of two Gaussians, and we follow this approach in our line profile analysis, comparing the statistical fit between a single Gaussian and double Gaussian. Line profile parameters are listed in Table 2 for STIS lines, and Table 4 for FUSE lines. In the case where two Gaussians were the better fit, we record the line profile parameters for each Gaussian.

There is a problem with the STIS pipeline for TIMETAG mode observations, in which the Doppler shift is not correctly applied.[6] The magnitude of the error is 3.8 pixels, or about 12 km s^{-1}, and degrades the intrinsic resolution of the spectra. Since our spectrum is accumulated over 4 orbits, we corrected for this effect by adding a Gaussian of width 12 km s^{-1} to the observed velocity width in quadrature to account for the decreased resolution. The observed line widths can then be expressed as the sum in quadrature of three velocities,

$$\left(\frac{\Delta\lambda}{\lambda}\right)^2 = 3.07 \times 10^{-11} \left(\frac{2k_B T_{\mathrm{max}}}{m_i} + \xi^2 + v_{\mathrm{inst}}^2\right) \qquad (2)$$

adapted from Wood et al. (1997), where $\Delta\lambda$ is the line profile FWHM in Å, λ is the line center in Å, k_B is Boltzmann's constant in erg K^{-1}, T_{max} is the temperature at which the ion's ionization fraction peaks in K, m_i is the ion mass in g, ξ is the most probable nonthermal velocity in km s^{-1}, and v_{inst} is the instrumental broadening of 12 km s^{-1}. Figure 6 displays the trend of nonthermal velocity with formation temperature for the line profiles analyzed here. If the line profile can be divided into a narrow and a broad component, and the interpretation of the broad component is microflaring, then the "quiet" atmospheric structures should be considered apart from the microflaring effects. On the other hand, if the entire line profile can instead be described by a normal distribution of line widths (as implied by Wood et al. 1996) then the entire line flux should be used, since the emission is integrated over the disk of the star. We note that apart from Si III λ1206, the narrow components of the two Gaussian fits are consistent with the thermal line widths.

Both O VI lines in the FUSE spectra are clearly skewed with the emission peak shifted shortward of the line centroid and with emission extending further in the longward wing than for the shortward wing. A single Gaussian fits the bulk of the 1032 Å line profile reasonably

---

[6] The problem has been corrected in CALSTIS version 2.15c; see http://www.stsci.edu/hst/stis/calibration/pipe_soft_hist/update215c.html and Herczeg et al. (2005) for more details.

and gives a line flux similar to that from direct integration with a line width (FWHM) of 0.16 Å, or 46 km s^{-1} width. One of the highest temperature transitions in the STIS spectra, N V, has one line profile (λ1238), statistically better fit by two Gaussians, while the other line profile (λ1242) is statistically better fit by one Gaussian. Lines from a resonance doublet are formed in a 2:1 ratio with same intrinsic line profile, so it is odd that only one N V transition shows evidence for two Gaussians. We compare the line profiles in Figure 7 to examine the reality of the second Gaussian in the λ1238 line. Since this line is brighter than its sister transition by a factor of two, the absence of evidence for a second Gaussian in the wings of the λ1242 line may simply reflect the poorer S/N; the two Gaussians which fit the λ1238 line are compatible with the flux-scaled λ 1242 line profile.

Wood et al. (1996) noted that the discrepancy between the widths of the O IV] intersystem line, a low opacity transition, and N V, which is a strong scattering line, in the active star HR 1099 suggests that these lines are not originating entirely from the same regions, despite the fact that the temperatures at which the lines are formed are nearly identical. In contrast, the widths of narrow component features in EV Lac are similar to those deduced from single-Gaussian fits to other transitions sharing the same formation temperature, indicating that the two are likely formed in the same regions and not subject to any strong scattering effects.

In the solar transition region, Jordan (1991) showed that the trend of nonthermal velocities with electron temperature increased as $\xi_{\rm turb} \propto T_e^{1/4}$. Dere & Mason (1993) determined that average nonthermal velocities in quiet regions of the Sun's atmosphere peak at ∼27 km s^{-1} at temperatures of 10^5K, and increase up to $\log T$ ∼5.5. Linsky & Wood (1994) found broad and narrow components for the Si IV and C IV transitions of the dMe flare star, AU Mic; the narrow components were characterized by nonthermal velocities of 15 km s^{-1} while the broad components averaged 97 km s^{-1}. In contrast, it appears that the trend of turbulent velocities in EV Lac's quiescent chromosphere–lower transition region, for lines with single Gaussian fits or the narrow component of lines fit by two Gaussians, *decreases* with increasing temperature above $\log T$ ∼4.8. These values appear to be subsonic, compared with typical nonthermal values inferred from the broad components of two Gaussians, which are mostly supersonic.

We explored the run of nonthermal velocities with temperature in the high S/N spectrum of another active M dwarf, AD Leo, during quiescent periods, to determine if the pattern seen on EV Lac is consistent with other active M dwarfs. This data is described in more detail in Hawley et al. (2003). The quiescent STIS spectrum of AD Leo was obtained using the same setup as for EV Lac, and also suffers from the 12 km s^{-1} Doppler correction error. The exposure time for AD Leo's quiescent spectrum is 52963 s. Line profile parameters were measured in the same way; i.e. one or two Gaussian line profiles were fit, and the line widths were interpreted as the sum in quadrature of a thermal width, nonthermal width, and instrumental 12 km s^{-1} width. The right hand panel of Figure 6 displays the trend of nonthermal velocities for AD Leo. The same lines, Si III λ1206, Si IV $\lambda\lambda$ 1393,1402, C IV $\lambda\lambda$1548,1550, and N V λ1238,1242 display evidence for two Gaussian profiles and show the same trend of broad component and narrow component velocities with temperature as EV Lac.

4. Electron Densities

We investigated the electron densities in the outer atmosphere of EV Lac by making use of density-sensitive line ratios in the X-ray and ultraviolet. The X-ray portion of the spectrum has numerous density-sensitive ratios in the forbidden to intercombination transitions of helium-like ions; the ions Si XIII, Mg XI, Ne IX, and O VIII are detected in either the MEG or HEG grating and can place constraints on n_e between 10^9 — 10^{14} cm^{-3} at temperatures of $\sim 2\times 10^6$–3×10^7 K. The ultraviolet portion of the spectrum also has density sensitive line ratios; for ease of interpretation, we choose transitions originating from the same ion, to separate density issues from temperature and abundance issues. We concentrate on transitions of O IV and O V; the ratios with the best signal to noise are O IV λ 1401.171/ λ1399.779, and O V λ1218.390/λ1371.292. These ratios place constraints for electron densities in the region n_e of 10^{10}- 10^{14} cm^{-3} at temperatures of $\sim 10^5$–2.5×10^5 K.

The theoretical line ratios are shown in Figure 8, along with the observed values and uncertainties. For the UV transitions we used theoretical ratios from CHIANTI v4.2 (Dere et al. 1997; Young et al. 2003); ratios for the X-ray transitions come from Porquet et al. (2001). Table 9 lists the transitions used in the density determinations, energy flux ratios, temperature at which the ratio was evaluated, and the corresponding density measurement and 1σ uncertainties (or upper limits). The electron density determinations are plotted in Figure 9 in the bottom panel.

The intercombination and forbidden transitions of Ne IX and Mg XI are blended, with Fe XXI and Fe XIX in the case of Ne IX and with the Lyman series limit of Ne X for Mg XI. Ness et al. (2004) and Testa et al. (2004) surveyed electron density diagnostics in X-ray spectra of a sample of active stars, including EV Lac. They used the entire accumulated observation for spectral analysis, whereas we have excluded large flaring events. The O VII and Ne IX estimates in Table 9 are slightly lower than those of Ness et al. (2004), while the Mg XI density estimate in Table 9 is slightly higher than the values given in Testa et al. (2004). We have not made explicit correction for the blending in the Ne or Mg lines, and our use of a subset of the observation makes our resulting error bars larger, but nonetheless there is good agreement within the error margins.

5. Differential Emission Measure Distribution and Abundances

The UV and X-ray line fluxes, along with the X-ray continuum, were used to constrain the shape of the differential emission measure distribution. This can be done using transitions for which the following assumptions are met:

1. The transition is formed in coronal equilibrium, i.e. a balance between collisional excitation and radiative de-excitation.
2. The transition is optically thin.
3. The transition is insensitive to changes in electron density.
4. The transition is detected with sufficient sensitivity in the spectrum, and is unblended with transitions from other elements or ionization stages.

In practice, many of our observed transitions from the upper chromosphere to the corona meet these criteria, and span three orders of magnitude in temperature. Figure 10 displays the temperature coverage of transitions in the STIS, FUSE, EUVE, and HETG spectra which can be used to constrain the DEM. Note that there is a gap in temperature coverage from $4{\times}10^5 K <$T$<10^6$K. In §5.1 we describe how we use the EUV and X-ray transitions (and the X-ray continuum) to compute the coronal DEM and abundances. Then in §5.2 we extend the temperature coverage to the transition region and upper chromosphere by using lines found in the UV and FUV. There are a few coronal transitions at these lower wavelengths (Fe XXI λ1354 and Fe XVIII λ978), but since the DEM at $\log T \geq 6.2$ is already constrained, we use these as consistency checks between the flux calibration and possible evidence of stellar variability (see § 3.2.4).

We constrained the choice of detected iron lines in the X-ray region to those which do not show evidence of density sensitivity; Smith et al. (2002) [7] compiled a list of density-sensitive X-ray lines between 1.2 and 31 Å, and marked those as density-sensitive which had standard deviations of greater than 10% of the mean emissivity, calculated at temperature grid points of $\log T(K)$ =6,6.5,7,7.5 and densities between 10^5 and 10^{15} cm^{-3}.

---

[7] Calculations can be found at http://cxc.harvard.edu/atomdb/features_density.html

5.1. Inverting the Chandra and EUVE Spectra: Coronal DEM and Abundance

We first examined the Chandra and EUVE spectra, and constrained the DEM in the temperature range $\sim 10^6$–3×10^7 (using the self-consistent treatment of line and continuum emission described in Osten et al. 2003). We define the DEM as:

$$\phi(T) = \frac{n_e n_H dV}{d\log T} \tag{3}$$

so that the observed line flux, f of an element i's ionic transition λ, can be expressed as $f_{\lambda,i} \propto A_i \int \phi(T) P_{\lambda,i}(T) d\log T$, where A_i is the abundance of element i, $P_{\lambda,i}$ is the emissivity of the transition, and $\phi(T)$ is the DEM. Once a guess at the DEM was made, using only iron lines present in the X-ray and EUV spectra, the abundances of N, O, Ne, Mg, and Si relative to Fe were determined, and the abundance of iron with respect to hydrogen was determined by using the shape and level of continuum emission in the X-ray to constrain the Fe/H ratio. Errors on the abundances relative to iron reflect the signal to noise statistics of the emission lines, while the error on the iron to hydrogen ratio was calculated by Monte Carlo simulations, perturbing the continuum flux values a random fraction of the noise level and recalculating the Fe/H ratio – the uncertainty in the Fe/H ratio is the 1 σ value of the resulting distribution of Fe/H values. Abundances of other elements with respect to hydrogen were then calculated, propagating both sources of error. The DEM at coronal temperatures and derived coronal abundance pattern are plotted in Figure 11, and Table 7 lists the derived metal abundances.

5.2. DEM and Abundances from Chromosphere through Corona

5.2.1. DEM

The DEM was then solved for iteratively, using all lines detected in the EUV and X-ray spectra, along with transitions determined from UV and FUV spectra (which include a few coronal transitions). The emissivities were calculated in the low density limit, using APEC (Smith et al. 2001), and any density-sensitive lines were excluded from this portion of the analysis. We attempted to minimize the ratio f_{obs}/f_{pred} for all transitions used. The APEC code incorporates atomic data from the CHIANTI project; we used a pre-release update which incorporates the most recent version of CHIANTI v4.2 (Dere et al. 1997; Young et al. 2003). As discussed in Del Zanna et al. (2002) and §5.3, there appear to be discrepancies for Li- and Na- isoelectronic sequences (N V, O VI, C IV, Si IV) so we relied more heavily on other transitions. We computed the effective temperature of each transition, taking into account the effect that the shape of the DEM has in skewing the dominant plasma which the transition experiences. The effective temperature is computed as

$$\log T_{\rm eff} = \frac{\int P_\lambda(T_e)\phi(T_e)\log T_e dT_e}{\int P_\lambda(T_e)\phi(T_e)dT_e} \tag{4}$$

where $P_\lambda(T)$ is the plasma emissivity and $\phi(T)$ is the DEM. The volume emission measure (VEM) was estimated by integrating the DEM in each $\Delta \log T$ =0.1 bin, and the volume occupied by the plasma was estimated at temperatures where electron densities could be constrained (§4) – the resulting volume estimates ($V \propto VEM/n_e^2$) are plotted in Figure 9.

5.2.2. Abundances

Our measurements of coronal abundances in EV Lac agree well with those determined from XMM-Newton observations by Robrade & Schmitt (2005). The X-ray luminosity determined from their RGS spectrum was 4.26×10^{28} erg s^{-1} (5–35 Å), which is higher than our X-ray luminosity of 1.8×10^{28} erg s^{-1} (1.8–26 Å). The XMM-Newton observation also included several flares, and the RGS spectrum appears to include both flaring and quiescent time intervals, which would explain the higher luminosity. Despite the $\sim$ factor of two change in luminosity, the overall characteristics of the spectra (dominant temperatures, abundances) appear similar.

In general there is overlap between elements whose ionic transitions appear in the coronal spectra and those ionic transitions appearing in the UV/FUV spectra; Figure 10 illustrates the temperature coverage and element distribution of the lines in the present analysis. The element carbon is the only element which we cannot constrain using our coronal spectrum, since the helium- and hydrogen-like transitions occur at $\lambda >$30 Å. It is not known whether the elemental abundance behavior found in the corona continues to lower temperatures. The photospheric abundances of EV Lac are not severely depleted (Reid et al. 1995; Gizis 1997) but could be mildly depleted. We examined flux ratios of two sets of oxygen and nitrogen lines to investigate the abundance ratios in the corona and transition region. Tables 2 and 6 indicate that O V and N V have nearly the same $T_{\rm eff}$, and O VII and N VII have identical values of $T_{\rm eff}$. By combining the observed flux ratios with the DEM-weighted emissivity ratios, a constraint on the abundance ratio in the corona and transition region can be made: assuming that the error in observational flux measurement dominates, we find:

$$\left(\frac{A_O}{A_N}\right)_{TR} = \frac{f_{O\ V}}{f_{N\ V}}\left(\frac{\int P_{N\ V}(T)\phi(T)d\log T}{\int P_{O\ V}(T)\phi(T)d\log T}\right) \tag{5}$$

$$\left(\frac{A_O}{A_N}\right)_C = \frac{f_{O\ VII}}{f_{N\ VII}}\left(\frac{\int P_{N\ VII}(T)\phi(T)d\log T}{\int P_{O\ VII}(T)\phi(T)d\log T}\right) \tag{6}$$

where e.g. $P_{\rm O\ V}(T)$ is the emissivity of the O V transition, and e.g. $f_{O\ V}$ is the observed flux of the transition of O V. Combining the line fluxes and emissivities, we determine $(A_O/A_N)_{TR}$ =0.2±0.03 and $(A_O/A_N)_C$ =0.6±0.2. These ratios are with respect to the solar photospheric abundances of Grevesse & Sauval (1998, 1999). This implies an enhancement of the coronal abundances by about a factor of three compared to the transition region. Nitrogen and oxygen have nearly the same FIP (14.5, 13.6 eV for N, O respectively) and do not display any differential behavior in the Solar corona compared to the lower atmosphere (Feldman & Laming 2000), so we would not expect to see any large difference in the ratio in EV Lac if it behaves like the Sun. There is a systematic effect which appears to affect transitions of Li- and Na-like isosequences, however (see §5.3 and Table 10), in which the observed flux for N V is 2–5 times the flux predicted using the DEM and emissivities, depending on which abundance patterns are assumed to occur in the transition region, as well as the role of dynamics in line formation. Since the origin of this effect is unexplained, and is of the same magnitude as the abundance ratio (but working in the opposite direction), it is not possible to determine for certain whether abundance gradients exist in the outer atmosphere of EV Lac. We considered two alternatives regarding the elemental abundance behavior in the outer atmosphere of EV Lac.

The first possibility was that the same abundances which exist in the corona also exist in the chromosphere (and possibly into the photosphere as well). To model this, we took the coronal elemental abundances, and applied that to the lower temperature transitions in computing predicted fluxes from the DEM. For C, we found it necessary to reduce the abundance to force the observed fluxes to agree with those predicted from the DEM using other elements. The carbon abundance value which minimized the χ^2 statistic between observed fluxes and those predicted from the DEM using all transitions of carbon in the STIS and FUSE spectra, was 0.45 Solar. Excluding the C IV transitions, which appear to have some undetermined discrepancies (see §5.3), increases the abundance depletion to approximately 0.35 times the solar photospheric value.

The second possibility is that EV Lac is similar to the Sun. Chemical fractionation in the solar atmosphere can be found at temperatures above 2.5×10^4K (Feldman & Laming 2000), and there is no reason to expect that the outer atmosphere of EV Lac has the same abundance pattern at all temperatures. In order to accommodate this, we introduced a hybrid abundance pattern, using our coronal abundances above 10^6K, and the solar photospheric abundances of Grevesse & Sauval (1998, 1999) below 10^6K. We note that the Del Zanna et al. (2002) investigation of AU Mic only used coronal iron line diagnostics, so they were not able to determine if coronal abundance anomalies existed, or explore the possibility of an abundance gradient between coronal and photospheric abundances.

The observed flux of an emission line is proportional to both the elemental abundance and the differential emission measure. It is well known in the solar outer atmosphere that an abundance fractionation mechanism exists, which depends upon the first ionization potential (FIP) of the element: those with a FIP less than 10 eV are preferentially enhanced in the corona compared with those having a FIP greater than 10 eV (see Feldman & Laming 2000, for a review). The interplay of the abundances and DEM are important because both tie into estimating the radiative losses of the upper atmospheric material. Figure 12 shows the estimates of radiative losses in EV Lac's atmosphere using the two abundance scenarios with the radiative losses from solar photospheric abundances, and the solar abundance fractionation described in Feldman & Laming (2000). The radiative loss function has been calculated here from the APEC database, and correcting the emissivities in those databases to the abundances of Grevesse & Sauval (1998, 1999). At a given temperature, the emissivity from lines and continuum are summed, then multiplied by the appropriate atmospheric abundance being assumed.

5.2.3. DEM and Abundances

Figure 13 displays the resulting DEM, and agreement between observed and predicted line fluxes, for transitions used in this analysis. Overall there is good agreement between the general shapes of the two DEMs: the hybrid abundance case has a slightly deeper trough at a temperature of $\sim 1.6\times10^5$K, which is due to the higher abundances. The temperature range over which the two DEMs differ most significantly is $5.3\times10^4 < T(K) < 2.7\times10^5$, with a maximum difference of less than a factor of 4 in a given temperature bin. Table 10 lists the ratio of observed to predicted flux for lines in the Li- and Na- isoelectronic sequences (N V, O VI, C IV, Si IV). For both abundance cases, the fluxes are underestimated, but by differing amounts. The magnitude of the coronal fractionation pattern is not severe, as the elements are depleted by factors less than 4. Thus we cannot conclude whether there is an indication for EV Lac's chromosphere or transition region to be metal-depleted as is found in the corona. Lacking any other constraints on the atmospheric abundance patterns, we cannot say which model is preferred, and consider both alternatives in subsequent sections.

5.3. Discrepancies in the Li- and Na- Isoelectronic Sequences

In §5.2.1 and §5.2.3 we mentioned the discrepancy between lines in the Li- and Na- isosequences and transitions arising from other isosequences in determining the DEM: the predicted flux is systematically less than that observed for the Li- and Na- isosequences. In §3.3 we described how the line profiles of several strong lines, notably the discrepant lines of C IV, N V, and Si IV, display evidence for two Gaussian features in the line profile; the narrow component has been interpreted as a quiescent line profile, while the broad component is due to micro-flaring. We tested the effect that selectively using the narrow component flux or both narrow and broad component fluxes had on producing agreement with the fluxes predicted from the DEM. Table 10 displays the change in agreement between observed and predicted flux when only the narrow component integrated line flux is used, for the two abundance cases. The DEMs used are those solved for in the previous section, so the only parameter being changed is the observed flux. For the lines originating from Li- and Na- isoelectronic sequences the reduction in flux makes the agreement better, but not perfect. Si IIIλ1206 is included because it shows evidence for two Gaussian line profiles, but has the opposite behavior in $f_{\rm obs}/f_{\rm pred}$.

This discrepancy has been addressed for several decades in interpreting solar transition region spectra. Allowing for density-dependence of the ionization fraction could remove some, but not all, of the discrepancy. Del Zanna et al. (2002) suggested the origin had to do with the temperature corresponding to the peak emission for these ions. We note that the current calculations being used for the stellar case are the ionization equilibrium calculations of Mazzotta et al. (1998), done in the low density limit. Based on solar work, we might expect that some of the discrepancy may be removed by considering the density-dependence of the ionization fractions, particularly as EV Lac's quiescent transition region densities are higher than typical quiet Sun transition region densities (Cook & Nicolas 1979). This approach is used in a recent work by Sim & Jordan (2005) who note that the high transition region pressures reduce the dielectronic recombination rate by merging the highly excited states into the continuum; the effect is to move the ionization balance to lower temperatures.

These two isosequences have long timescales due to recombination from He-like and Ne-like (closed shell) ionization stages, and so also could be more responsive to non-equilibrium effects. Judge et al. (1995) suggested that diffusion of ions due to steep temperature gradients in the transition region could explain the observed behavior. Wikstol et al. (1998) explored the properties of dynamic plasmas from their emitted spectra, and concluded that a number of erroneous conclusions could be drawn by making the assumption of an intrinsically static atmosphere. Because of the steep temperature gradient in the transition region, these zones respond dramatically to the passage of waves, with large redshifts and blueshifts due to compression and relaxation. This could be observed as extra broadening in transition region lines averaged over many wave passages.

As discussed in Hawley et al. (2003) for UV flares in AD Leo, these transitions are also the brightest and show the most response to large flares. Weaker transitions don't show as large a flare response. The observed broadening (and discrepancy) may therefore be related to micro-flaring, and reflect a non-equilibrium situation. This could be addressed by detailed calculations of the dynamical response of a flare-heated atmosphere. This explanation cannot account for the Si III transition at 1206 Å, which also shows broad components, but belongs to a different iso-sequence (similarly for C III transitions in the FUSE bandpass, which show broad components in other active dwarfs; Redfield et al. 2002). Nor does the O VI doublet, where no broad components are found, fit this scenario, although broad components have been found in O VI transitions in other active dwarf stars (Ake et al. 2000; Redfield et al. 2002).

6. Discussion: Inferring Atmospheric Properties

We determined several fundamental quantities — n_e, A_i, and the DEM — in §4 and §5 which describe the atmosphere. Now we turn to computing the atmospheric properties based on these measurements.

6.1. Electron Pressures

The bottom panel of Figure 14 displays the dependence of electron pressure on electron temperature calculated from density-sensitive ratios in §4. We combine these estimates of the electron pressure with turbulent pressure in estimating the total pressure at different points in EV Lac's transition region and corona. Upper chromospheric and transition region line profiles show excess broadening, interpreted as nonthermal turbulent velocities (ξ) and discussed in §3.3. We estimate the magnitude of the turbulent pressure using the following equation:

$$Y = \frac{P_{\rm turb}}{P_{\rm gas}} = \frac{\mu m_p}{2k_B T}\xi^2, \tag{7}$$

where $\mu = 1.4X/(1+1.1X)$ is the average particle mass, $X = n_H/n_e$, $\mathrm{P}_{\rm gas}$ is the gas pressure (related to electron pressure P_e via $\mathrm{P}_g = P_e(1 + 1.1X)$ (from Jordan 1996)). The middle panel of Figure 14 displays the amount of turbulent pressure at temperatures where line broadening indicates nonthermal velocities. The largest ξ at these temperatures is used to compute the maximum amount of total pressure, including turbulence, in the upper chromosphere through the corona. The top panel of Figure 14 displays the run of total pressure with temperature. This was computed two ways, with no turbulent pressure (gas pressure only) and with the maximum amount of turbulent pressure indicated from line widths. Although the data are sparse, there is an implied disconnect between the transition region pressures, roughly constant, and the coronal pressures, which increase sharply with temperature.

Using equations in Jordan (1996) and Griffiths (1999), we investigate the run of pressure in the atmosphere using the emission measure distribution, and a reference pressure, assuming the transition region and corona are in hydrostatic equilibrium, and using a spatially uniform plane-parallel approach. For total pressure (defined as the sum of gas and turbulent pressures)

$$P^2_{\rm tot}(T) = P^2_{\rm tot,ref} \pm 8.5 \times 10^{-40} g_\star \int_{T_{\rm ref}}^{T} CEM0.3(1+1.1X)^2(1+Y)dTe \qquad (8)$$

where $Y = P_{\rm turb}/P_{\rm gas}$. The DEM is converted to column emission measure (CEM; $\int n_e n_H ds$) via:

$$\int n_e n_H ds = \frac{\int \phi(T) d\log T}{4\pi R^2_\star} \qquad (9)$$

where R$_\star$ is the stellar radius, and the assumption is that the emission is spherically symmetric (ds is a radial path length). The CEM is regridded so that it is expressed as CEM0.3, which in the notation of Jordan (1996) is

$$CEM0.3(\log T) = \int_{\log T-0.15}^{\log T+0.15} n_e n_H ds \qquad (10)$$

the $\Delta \log T$ =0.3 arises because emission lines are typically formed over a temperature range of $\Delta \log T$ =0.3. The reference total pressure used is 6.5 dyne cm^{-2}, determined at $\log T$ = 5.4, and consistent with the upper limit at $\log T$ =5.2; we assume that lower in the atmosphere the pressure is constant (except where P$_{\rm turb}$ measurements suggest additional pressure support). The EM modeling indicates an almost flat $P(T)$ profile which is not consistent with the observed coronal pressures.

For temperatures above 6×10^{5}K, the estimated trend between electron pressure and temperature using the Rosner et al. (1978) scaling laws are displayed, for loop lengths of 10^8 – 10^{10} cm. This treatment assumes that the coronal loops are hydrostatic, constant pressure with maximum temperature at the top of the loop, with the heating scale length greater than or equal to the loop scale size. The high pressures in the corona can only be accommodated by small loops (10^8 cm or smaller) and still cannot explain the large jump in pressure at $\log T = 6.9$.

The steep increase in total pressure implied by the observed coronal electron densities in Figure 14 cannot be ascribed to the consequences of hydrostatic equilibrium. Neither the emission-measure modeling nor the loop scaling laws are able to reproduce the observed coronal pressures, except for extremely small loop sizes (10^8cm, or $\sim 0.004 R_\star$) and only in the lower corona — the observed electron pressures near 10 MK are too high. Figure 14 also displays the magnitude of the magnetic field strengths required to magnetically confine the plasma: at the highest coronal temperatures (> 8MK), field strengths of up to 1kG are required.

6.2. Timescales

Combining the radiative loss function calculated above with the run of electron density versus temperature calculated in §4, we can calculate the radiative loss timescale, $\tau_{\rm rad}(T_e)$,

$$\tau_{\rm rad}(T_e) = \frac{3(T_e) k_B T_e}{n_e(T_e)\psi(T_e)} \tag{11}$$

where $n_e(T_e)$ is the electron density at a given electron temperature T_e, $\psi(T_e)$ is the radiative loss function (units erg cm^3 s^{-1}), and k_B is Boltzmann's constant. We interpolated the observed values of $n_e(T_e)$ onto a finer grid with $\Delta \log T = 0.1$ spacing between $\log T = 5$ and 7. We assumed the atmosphere at temperatures below 10^5K was at constant pressure to extrapolate the radiative loss function to lower temperatures; the density estimates from O IV and O V appear to confirm this. We also computed the timescale for conductive losses using different estimates for loop lengths, based on van den Oord et al. (1988)

$$\tau_{\rm cond} = \frac{3 n_e k_B L^2}{\kappa T_e^{5/2}} \tag{12}$$

where κ is Spitzer conductivity coefficient ($=8.8\times10^{-7}$ erg cm^{-1} s^{-1} K$^{-7/2}$, Spitzer 1962), L is the loop length scale. The geometric mean of the two, $\tau_{\rm geo}$, is

$$\frac{1}{\tau_{\rm geo}} = \frac{1}{\tau_{\rm rad}} + \frac{1}{\tau_{\rm cond}} \tag{13}$$

The dependence of $\tau_{\rm rad}$ and $\tau_{\rm cond}$ on electron temperature between these temperatures is depicted in Figure 15. The two loop length estimates are based on L of 10^8 and 10^9 cm derived from the pressure-temperature scaling discussed in Section 6.1. The total timescale in the transition region and corona is between 10 and 1000 s, which is small compared to the timescale for solar coronal radiative losses, $\sim 10^4$s (Golub et al. 1989). The depression in radiative losses from EV Lac's corona compared to the Solar corona, due to abundance depletion, is more than compensated for by the high inferred electron densities, and the timescales for radiative loss are consequently short. For the shorter loop length inferred here, the conductive timescale is shorter than the radiative timescales. The dependence of conductive timescale on loop length is L^2 so conductive timescales rise rapidly with an increase in loop length. In order for the corona to maintain its quiescence, the heating timescale must be of the same order as the timescale on which energy is lost. This implies that there must be significant continued heating for the corona to maintain its quiescence.

6.3. Energy Balance

Because we have measured the DEM from the upper chromosphere to corona, we can use it and the observational constraints on pressures to investigate how much energy is being lost and therefore how much is required to heat the corona. In the absence of flows, the atmosphere at each point is in a balance between radiative and conductive losses, and mechanical heating. We estimate the magnitude of each of these terms, using

$$\nabla \cdot F_c + \nabla \cdot F_r = \nabla \cdot F_h \tag{14}$$

where radiative losses F_r are estimated as

$$F_r(T_e) = \int n_e n_H \psi(T_e) ds, \tag{15}$$

and the classical expression for conductive losses is

$$F_{c,cl}(T_e) = -\kappa T_e^{5/2} \frac{dT_e}{ds}, \tag{16}$$

where ds is the emitting region. The equation defining the emission measure distribution can be re-written to describe the temperature stratification,

$$\frac{dT_e}{ds} = \frac{n_H}{n_e} \frac{P_e^2}{\sqrt{(}2)T_e CEM k_B^2} \tag{17}$$

from Jordan (1996), where all quantities except temperature are assumed to be constant over the region of line formation, and a plane-parallel atmosphere is assumed. The classical expression for conductive flux uses the Spitzer conductivity times the local temperature gradient to approximate the heat lost. However, a limiting value of the conductive flux occurs when the electrons are free-streaming, in which case the saturated conductive flux can be written as

$$F_{c,sat} = sgn(F_{cl}) \frac{n_e (k_B T_e)^{3/2}}{4\sqrt{m_e}} \tag{18}$$

where F_{cl} is the classical expression. The classical conductive fluxes in the corona become unphysically large, due to the high coronal pressures discussed in §6.1 through the P_e^2 dependence of dT_e/ds. At most temperature bins above $\log T$ =5., the conductive fluxes exceed the saturated levels, the maximum being in the corona, by factors of up to 10^3. Following the discussion in Smith & Auer (1980) and Fisher et al. (1985), we compute the following expression for evaluating the conductive fluxes:

$$F_c = \frac{F_{c,cl}}{1 + F_{c,cl}/F_{c,sat}} \tag{19}$$

which has the advantage of achieving the limit $F_c \rightarrow F_{c,cl}$ when $F_{c,cl} \gg F_{c,sat}$ and $F_c \rightarrow F_{c,sat}$ when $\mathrm{F}_{c,cl} \ll F_{c,sat}$. We ignore anomalous heat conduction due to ion-acoustic instability.

Our goal is to compare the run of radiative and conductive losses with temperature, so we compute divergences of the analytic expressions above (see Appendix). We have assumed n_H/n_e is constant over the temperatures being considered here. An estimate of radiative losses has been calculated using the two scenarios for abundance patterns in the outer atmosphere, and conductive losses are computed using the resulting DEMs.

At temperatures below $10^{5.2}$K where our density diagnostics are insensitive, a constant pressure equal to that derived at $\log T$ =5.2 and 5.4 was used. We do not calculate the radiative and conductive losses above 10^7K, as our pressure estimates end there. The left panels of Figure 16 displays the run of radiative and conductive fluxes with temperature from the upper chromosphere through the corona for the DEMs determined using the coronal and hybrid abundance patterns. At temperatures $\log T \leq$6.7 the energy loss rates due to radiation exceed those from conduction. However, at higher temperatures the opposite occurs. This result depends ultimately on the high values of n_e at these high temperatures; reducing n_e by an order of magnitude (equivalent to the Mg XI diagnostic being in the low density limit) has a hundred-fold effect on decreasing the conductive loss rates.

Figure 16 compares the analytic derivation of radiative and conductive losses with those of preflare numerical calculations of Allred et al. (2005). The numerical calculations were derived by using a modified form of the Spitzer conduction formula, with a saturation limit imposed to avoid unphysically large fluxes from the steep temperature gradient. The radiative losses show almost no agreement between analytic and numerical calculations. This has to do with the difference between the observed DEM and the amount of material at high temperatures which went into the numerical calculations. The analytic evaluation of conductive fluxes likewise show a peak at $\log T$ =5, whereas the numerical results show conductive losses peaking at lower temperatures. The difference may similarly relate to the DEM, whereas above $\log T$ =6.4 it most certainly is related to the jump in pressure inferred from the observations.

The energy heating rate at each temperature can be estimated under the assumption of energy balance by adding the energy loss rates due to conduction and radiation calculated above. This is shown in Figure 16 for the two abundance scenarios. As pointed out by Cram (1982), the large X-ray fluxes of dMe stars coupled with the assumption of isotropic assumption means that there is a large X-ray flux directed downward into the atmosphere, which may result in an appreciable amount of heating of the upper chromosphere/transition region. However, recent calculations of the X-ray and EUV backwarming taking place during stellar flares (Allred et al. 2006) show that this contributes a negligible amount of heating.

In the low-temperature corona, there is a local enhancement in the heating rate which peaks at $\log T$ =6.4. This is due to the increase in radiative loss rate from the peak in the DEM at these temperatures. The sharp jump in energy heating rate at higher temperatures is a consequence of the large conductive loss rates at the higher temperatures, which is itself driven by the dramatic rise in pressure deduced from density-sensitive line ratios. We can use the emitting volume estimates presented in §5.2.1 and Figure 9 and the volumetric heating rates to determine the power input. In the transition region at $\log T$ =5.4, the emitting volume is $\sim 10^{26}$ cm^3 ($\Delta \log T$ =0.1), with an energy heating rate of $\approx 9\times10^4$ erg cm^{-3} s^{-1}, for a total power input of $\approx 9\times10^{30}$ erg s^{-1}. At $\log T$ =6.4, the emitting volume of 10^{30} cm^3 coupled with the heating rate of 7×10^6 erg cm^{-3} s^{-1}, implies 7×10^{36} erg s^{-1} of power input. At $\log T$ =6.9, there is an emitting volume of 10^{25} cm^{-3} and heating rate of 6×10^{10} erg cm^{-3} s^{-1}, for a needed power input of 6×10^{35} erg s^{-1}. It is remarkable that despite the large differences in loss rates, these are within an order of magnitude of each other. The $\sim$ 7 orders of magnitude difference between the observed X-ray luminosity of $\sim 10^{28}$ erg s^{-1} and the total power required to heat the corona underscores how inefficient radiation alone is in diagnosing the required energy inputs. A possible next step would be the investigation of loop models to explain the above results in terms of atmospheric structure. The calculations in this section imply that a large amount of energy must be deposited at high temperatures, which if realistic, would be hard to envision under a static energy balance scenario. In particular the large conductive loss rates and the steep temperature gradients in the corona imply that a dynamic situation leading to mass flows is inevitable. Thus we look to alternative explanations in the following section.

6.4. Flare Heating

This treatment is fundamentally different from the energy balance arguments applied above, since a flare-heated atmosphere has mass flows, shocks, particle beams, etc. A correct treatment requires a comprehensive flare theory which could account for all the processes known to occur in both collisional plasmas (e.g. chromospheric evaporation and coronal heating, coronal plasmoid ejections) and collisionless plasmas (e.g. particle acceleration, particle beaming), and then combines them in an ensemble average over a flare distribution to truly describe a flare-heated atmosphere. Since this is still not possible even for single solar flares, we resort to statistical arguments.

6.4.1. DEM Considerations

Güdel et al. (2003) studied the statistical distribution of coronal flares and their effect on the distribution of plasma with temperature in the corona, under the assumption that the coronal heating could be accounted for entirely by a superposition of flares proceeding to smaller and smaller energies (the so-called "nanoflare heating hypothesis"). Following the arguments outlined in their section 6.4, the shape of the DEM can be used as a diagnostic for flare-heated coronae: at temperatures above the maximum DEM, the decreasing slope can be used to determine α, the power-law index of the flare frequency-energy relation. The DEM (Figure 13) appears to have a maximum at $\log T$ =6.4, and we measure a slope from $\log T$ =6.4–7.3 of ~ -0.6. Using the parameter values discussed in Güdel et al. (2003) and our measured high temperature DEM slope, this implies $\alpha \approx$2.2. For values of $\alpha > 2$, flares are numerous enough to provide the observed X-ray luminosity. The quiescent DEM and this model therefore imply that EV Lac's quiescent corona can be described by a multitude of small-scale flaring events. This is not a self-consistent treatment of flare-heated coronae, only a demonstration that the corona can be interpreted in light of mechanical heating due to flares.

6.4.2. Comparison of Flare/Non-Flare Quantities

We investigated the temporal variability in the X-ray observation to examine whether there was any difference in behavior of high temperature and low temperature coronal plasmas, as might be observed if the high temperature component were due to a superposition of flaring activity. The two strongest lines in the X-ray spectrum are Ne X λ12.14 and O VIII λ18.97, corresponding to $\log T_{eff}$ =6.7 and 6.4, respectively. We extracted spectra in two hour time bins, and performed Gaussian line fits to the spectra, recording the width, wavelength of line center, and line flux (see Figure 17). There is no evidence for the high temperature line being more variable than the low temperature line, although the large error bars on particularly the O VIII flux hinder a more conclusive result. An inspection of the spectrum (Figure 5) reveals that longward of 17.4 Å, most strong transitions are characterized by $\log T_{\rm eff}$ <6.5, and shortward of 17.4 Å, the opposite case holds. We made light curves of soft (17.4< λ <25 Å) and hard (2< λ <17.4 Å) photons in 1000 s bins. Enhancements are more noticeable in the hard light curve during large-scale flares, but there is no evidence for more variability in the hard light curve outside of large-scale flares. We confirmed this statistically by comparing the means and variances of the soft and hard light curves outside of times of large-scale flares.

Mitra-Kraev et al. (2005) examined UV–X-ray correlations during flares from a sample of dMe stars observed with XMM-Newton, and found that a comparison of X-ray to UV energy loss rate ratio during flares was similar to that obtained outside of flaring times, suggesting a common origin. Since the entire outer atmosphere, from photosphere through corona, is involved in the flare, the hypothesis of flare-heating providing the energy requirements of the corona necessitates a difference in scaling law relationships for stars where flare-heating is viable. However, the variations induced by large-scale flares and our inability to explain those multi-wavelength correlations in individual cases hampers an attempt to say anything conclusive about a relationship between time-averaged quantities and quantities deduced from individual flares. A statistical study of flux ratios in active stars compared to the subset for which flare-heating is a viable hypothesis must be done to tease out any differences.

If the quiescent coronal material is heated through a flare-related process which dredges material from lower in the atmosphere through an evaporation process, then we should expect to see a correspondence between coronal abundances and those in the chromosphere where evaporation is presumed to occur. Further, if the physical processes which occur during flares scale with flare parameters (e.g. flare energy), then large-scale flares should be able to diagnose processes occuring during the smaller scale flares which are hypothesized to provide the quiescent luminosity. The large X-ray flares in this Chandra observation, discussed in Osten et al. (2005), show no evidence for abundance enhancements. However, some large stellar flares studied in detail show evidence of abundance enhancements (Osten et al. 2003), implying some degree of complexity to both the flare process and the relationship between flares and flare-heated quiescent conditions.

7. Radio Emission at High Frequencies

The negative spectral indices at frequencies higher than 5 GHz points to partially optically thin emission. In this section we consider sources of the emission and the implications for coronal structure. The high frequency radio spectra of some active M stars has been inferred to provide evidence of gyroresonance emission (Güdel & Benz 1989), and we address the possible emission mechanisms contributing at our highest frequency, 15 GHz. The three most plausible are: (1) nonthermal gyrosynchrotron emission from accelerated electrons; (2) gyroresonance emission, and (3) free-free emission. The last will be present at all frequencies, and represents the limiting value of stellar radio emission fluxes. The optical depths of these mechanisms scale as:

$$\tau_{NT} \sim n_{\rm tot} B^{2.3+0.98\delta} \tag{20}$$

$$\tau_{gr} \sim T^{s-1} n_e \tag{21}$$

$$\tau_{ff} \sim \frac{CEM}{T^{3/2}} \tag{22}$$

$$\tag{23}$$

where $n_{\rm tot}$ is the total number density of accelerated electrons, B is the magnetic field in the source, δ is the index of the nonthermal electron density distribution, s is the harmonic number, and CEM is the emission measure distribution (Dulk 1985). These estimates assume a homogeneous source.

For gyroresonance and free-free emission, we have computed the expected optical depths assuming that the quantities derived from our spectral observations in §4 and §5 apply to the source regions of radio emission. Figure 18 displays the optical depths, calculated using equations (1) and (3) in Leto et al. (2000). Based on the emission measure distribution, at 6 cm, the free-free emission should approach optical depth unity in the low temperature corona. At temperatures below 10^5K the expected free-free emission optical depth rises above unity, as expected. The expected contribution of optically thin free-free emission from transition region and coronal plasma ($\log T \geq 5$) to the observed radio emission is small, however; only $\sim$40 μJy. The magnetic scale length L_B is the unknown quantity by which gyroresonant optical depths are scaled in Figure 18 and indicates that the two shortest wavelengths should also suffer from optical depth effects, at either the second or third harmonic of the gyrofrequency. Equating the observed frequencies with the harmonics of the gyrofrequency ($\nu = s\nu_B = 2.8 \times 10^{-3} Bs$ GHz) for $s = 2, 3$, we derive magnetic field strengths in the radio-emitting source of 2.7, 1.8 kG for $s = 2, 3$ at 15 GHz (2 cm), and 1.5, 1 kG for $s = 2, 3$ at 8.4 GHz (3.6 cm). These values are consistent with the equipartition magnetic field strengths required to magnetically confine the hot coronal plasma at temperatures >8 MK discussed in §6.1 and thus lend some credence to the existence of such strong magnetic fields in the corona. We emphasize, though, that these estimates are made for a homogeneous source. We estimate the optically thick emission due to gyroresonance emission following equation (5) in Leto et al. (2000) as

$$S = 810 \frac{T}{2 \times 10^7} \left(\frac{\nu}{15GHz} \right)^2 \left(\frac{R_s}{0.3 R_\odot} \right) \quad \mu Jy \tag{24}$$

for a heliocentric distance of 5 pc. Assuming an optically thick source size equal to 1.1 times the stellar radius of ≈ 0.3 $R_\odot$, we expect a flux density of ∼890 μJy at 15 GHz and ∼280 μJy at 8.4 GHz for emission at $T = 2 \times 10^7$K, the highest temperature revealed by the emission measure analysis (§5). This is higher than the observed flux density at 15 GHz and so is not consistent with the soft x-ray emitting source being spatially coincident with the radio-emitting source. Thus the high frequency radio emission is not consistent with being explained completely by gyroresonance emission, but spatial inhomogeneities in radio and/or soft X-ray (SXR) emitting regions may be account for some of the discrepancies.

For gyrosynchrotron emission from a homogeneous population of mildly relativistic electrons described by a power-law distribution in energy, the optically thin spectral index α can be related to the index of the power law, δ, by $\alpha = 1.2 - 0.895\delta$ (Dulk 1985). For a relatively hard distribution with $\delta = 2$, $\alpha = -0.59$, which is consistent with the 3.6–2 cm spectral index. However, the total integrated energy does not converge for such a hard electron distribution. If the radio emission is not completely optically thin at one or both of these frequencies (or includes contributions from gyroresonance emission, see paragraph above), this could lead to our inferred δ being smaller than the actual δ; thus we explore the effect of $\delta = 3$ in the following simple models of the magnetic geometry.

Constraints on coronal properties can be obtained by using simple analytic models, and a radial decrease in the number of nonthermal particles. We use the analytic formulae of White et al. (1989), who parameterized spatial inhomogeneities in the magnetic field and nonthermal number density distribution. White et al. (1989) considered a global dipole, which they termed a “bare” dipole, and a “buried dipole”, in which the depth below the surface at which the dipole is buried is much less than a stellar radius. The parameter m describes the power-law index of the radial dependence of the number density. The $m = 0$ case corresponds to a nonthermal electron distribution independent of radius, appropriate for an isotropic pitch angle distribution. The other extreme, $m = n = 3$, corresponds to the radial dependence of the electrons being the same as that of the dipolar magnetic field; this is the situation that would be obtained by conserving both particle and magnetic flux in the case of open field lines.

By constraining the index of the power-law distribution to be $\delta = 3$, we explored possible scenarios, including a global and buried dipole, the radial dependence of the nonthermal electron energy (either constant with radius, or having the same radial dependence as the magnetic field), the base magnetic field strength, and the total number density of accelerated electrons above a cutoff value.

For $\delta = 3$ and an observed flux density S_ν, the magnetic field strength at the base of the dipole and the total number density of nonthermal electrons are related as $S_\nu \propto n_{\rm tot} B^{2.5}$. The frequency at which the spectrum turns over is also a strong function of the magnetic field strength in the source. M dwarf radio spectra are consistent with a rising spectrum between 1.4 GHz and 5 GHz, and flat or declining flux density spectra at higher frequencies (White et al. 1989). The right panel of Figure 18 displays allowed regions of $n_{\rm tot}$ and B which produce the flux density at 15 GHz to within a factor of two, and have a spectral turnover between 2 and 8 GHz, to constrain some of the radio coronal properties of EV Lac. There is very little difference between the $m = 0$ and $m = 3$ models for a bare dipole. These models imply a relatively large base magnetic field strength and low value of total nonthermal electron density. We note that the magnetic field that Johns-Krull & Valenti (1996) observed on EV Lac is almost certainly not a global dipole field: Polarization from optical observations is discussed explicitly in Valenti et al. (1998) where the authors argue that AD Leo's field is not a global dipole. Thus we considered dipoles buried at smaller depths, which would be characteristic of individual active regions. For a dipole buried to $0.2R_\star$ the base magnetic field strength can be relatively small ($\leq$ 100 G), but with a larger total nonthermal electron density ($\geq 10^9$ cm^{-3}).

8. Constraints on Coronal Structure

The multi-wavelength data described here pose a conundrum: the soft X-ray (SXR) observations require large magnetic field strengths in the hot corona to confine the plasma, but the radio observations do not support such large fields in the corona providing a significant amount of gyroresonant opacity. These two observations can be reconciled if the radio and SXR emission regions are not coincident. This conclusion was reached by previous authors who determined (White et al. 1994) that the hot component of the SXR-emitting plasma was not coincident with the strong magnetic fields in the low corona, and Leto et al. (2000) who estimated that the hot coronal material must be co-spatial with coronal magnetic fields less than 0.5–1 kG. The results described in this paper represent the first attempt at a realistic investigation of the problem, using high spectral resolution observations to determine the shape of the continuous emission measure distribution and place constraints on the electron density at several temperatures in the outer atmosphere of an active M dwarf. The coronal electron density determinations place an additional constraint: Any radio emission from the high temperature, high density soft X-ray-emitting material is below the local plasma frequency ($\nu_p \approx 9\sqrt{(n_e/10^{12} cm^{-3})}$ GHz) and therefore cannot propagate. For n_e =10^{13} cm^{-3} ν_p =29 GHz so the electromagnetic wave is damped. This is an additional argument that the high temperature X-ray emitting plasma cannot be spatially coincident with the centimeter-wavelength radio emission.

The volumes derived from the emission measure analysis imply remarkably compact coronal structures: for spherically symmetric coronal emission, V <10^{30} cm^{-3} and EV Lac's radius, the coronal extent is less than 0.1 $R_\star$. We estimate the filling factors for SXR and radio emission using our observations. For soft X-ray emission, we compare the observed V_X (deduced from VEM and n_e in §5.2) with the volume available for a spherically symmetric volume $V \sim 4\pi R_s^2 h$, where h is the height of the emission above the stellar photosphere and deduce a filling factor f_X,

$$f_X = \frac{V_{\rm X}}{4\pi R_s^2 h} \quad . \tag{25}$$

and we relate h to the loop length L by $h \sim L/2$. The volumes shown in Figure 9 display a large discrepancy between the plasma-emitting volume in the low temperature corona, $V_{\rm X}$ ~10^{30} cm^3, and that in the high temperature corona, $V_{\rm X}$ ~10^{25} cm^3. This is consistent with the other significantly different plasma characteristics of the low- and high-temperature corona discussed above. We thus derive two filling factors, for the ~2.5 MK plasma (LTC) and ~ 8MK (HTC) –

$$f_{X,LTC} = \frac{4 \times 10^8}{L_{LTC}} \quad f_{X,HTC} = \frac{4 \times 10^3}{L_{HTC}} \tag{26}$$

where L_{LTC} and L_{HTC} are the loop lengths for the low- and high-temperature coronal plasma, respectively. Filling factors of order unity are returned if loop lengths L_{LTC} ~few $\times 10^8$ cm, whereas dramatically smaller length scales are needed to obtain near unity filling factor for the high temperature coronal plasma. Conversely, this seems to indicate a much smaller than unity filling factor for the high temperature coronal plasma. An equivalent argument can also be made using the temperature gradient determined in §6.3 (equation 17) and determining a length scale l,

$$l = T/(dT/ds) \propto \frac{CEM}{n_e^2} = \frac{VEM}{n_e^2 4\pi R_s^2} \tag{27}$$

in which case for filling factor of unity, the loop length must be $\approx 1/l$.

We also estimate the filling factor for radio emission by using the results of resolved radio sizes from VLBI studies (Pestalozzi et al. 2000), and compare this with the volume deduced from optically thin emission, where $V_R = L_R/\eta$, L_R is the radio luminosity, and η is the emissivity for gyrosynchrotron emission, taken from Dulk (1985). We assume $\delta = 3$ and θ =45°. The VLBI observations cited were conducted at 3.6 cm, and determined a source size h_R of $\sim 2\times 10^{10}$ cm for YZ CMi (dM4.5e). We hereby assume that this is also a characteristic radio emission length scale for EV Lac. The total radio-emitting volume is then $V_{\rm tot}$=$4\pi R_s^2 h_R$, with h_R the resolved height of radio emission above the stellar radius. The observed radio- emitting volume is estimated from the radio luminosity and emissivity at 8.5 GHz (3.6 cm). The filling factor for gyrosynchrotron emission at 3.6 cm is thus:

$$f_R = \frac{V_R}{V_{\rm tot}} = \frac{3.4\times 10^{11}}{n_{tot} B^{2.48}} \tag{28}$$

where B is the magnetic field strength in the radio-emitting source, and n_{tot} is total number density of nonthermal particles. Based on the radio modeling in §7, a global dipolar model for the radio emission can accommodate B ∼20G, n_{tot} $\sim 10^6$ cm^{-3}, while a dipole buried to a smaller depth requires elevated number densities, n_{tot} $\sim 10^{10}$ cm^{-3} at similar magnetic field strengths. Using these numbers, we estimate f_R to be ∼200 for the global dipole and $\sim 2\times 10^{-2}$ for the buried dipole. A filling factor larger than unity is unphysical, and thus appears to be in agreement with the optical polarization limits ruling out a global dipolar component.

The results of this section and §6 imply different length scales for the cool and hot SXR-emitting plasma – the low temperatures should be more extended and therefore undergo more rotational modulation. The radio source is also inhomogeneous, with scale lengths larger than the expanded, low temperature coronal material, which would place the radio spectral results in agreement with the soft X-ray constraints. The radio source is also likely not coincident with the large field strengths inferred from optical observations, as the equatorial surface fields estimated from the simple dipole field geometry for gyrosynchrotron emission are in the range ∼30–500 G, and the filling factor times field strength derived from Saar (1994) and Johns-Krull & Valenti (1996) are ∼4 kG. The high temperature corona, from DEM arguments in §6.4.1, is likely related to a flare heating process. The high pressures derived for this plasma also imply that it is the most compact, with the smallest timescales for energy loss and the largest energy loss rates. The lifetime of accelerated particles to losses by collisions is 1s or less in the HTC, and only of order 100 times longer in the LTC. In order to maintain a stable, long-lived population of accelerated electrons which is observed as cm-wavelength radio emission, continual replenishment is necessary. If the flare process which heats plasma to high temperatures also involves the acceleration of particles, then there should be a link between radio emission from accelerated electrons and high temperature coronal plasma — although from the arguments above the two populations cannot be spatially coincident.

8.1. Comparison with Solar Coronal Structures

The high angular resolution and temperature discrimination of narrow-band filters available on the Transition Region and Coronal Explorer (TRACE) have been instrumental in making advances in understanding of solar coronal loop structures, heating and dynamics. EUV-emitting loops have temperatures generally from 0.8–1.6 MK, and thus are cooler than the temperatures discussed in this paper, but nevertheless the detail with which they have been investigated motivates this as a starting point for comparison. The lack of observed temperature variation along loop lengths (Lenz et al. 1999) in the solar corona as seen by TRACE has been interpreted as the signature of a highly filamentary corona (Reale & Peres 2000). Aschwanden et al. (2000) found nearly isothermal loop threads whose temperature gradients where much smaller than predicted by static, steady-state models for uniform loop heating. The loop base pressure was also higher than that predicted for static, steady-state models invoking uniform heating, and independent of loop length, implying a departure from such models. Aschwanden et al. (2000) showed that coronal heating was localized to altitudes less than 20 Mm, which is much smaller than the longest loop lengths ($\sim 3\times 10^{10}$ cm). This result suggests that short loops experience uniform heating, while long loops do not. The pressure scale height was found to exceed the hydrostatic scale height for all but the shortest of loops, supporting a conclusion that these loops are not in hydrostatic equilibrium. Neupert et al. (1998) showed that radiative losses exceed conductive losses by factors of 100. Comparison of results for EUV-emitting loops with studies of soft X-ray emitting loops suggests a physical distinction between the two. Priest et al. (2000) determined that a larger temperature gradient exists in soft X-ray-emitting loops, and they ruled out footpoint-dominated heating, preferring instead uniform heating.

Our conclusion calling into doubt the applicability of hydrostatic, steady-state loops appears to resonate with the results obtained from TRACE for solar coronal loops, albeit for markedly different temperatures. However, other aspects of coronal structures on the Sun and EV Lac appear vastly different. The temperature gradients inferred from an analytical treatment of the spatially integrated emission (assumed spherically symmetric) in EV Lac suggest that at low temperatures in the corona, T$\sim$2.5MK, the gradient will be small, $\sim 10^{-2}$ K/cm. But the temperature gradient appears to increase by a factor of $\sim 10^{6}$K over a range of 3 in temperature. This would presumably place severe requirements on the types of structures and heat inputs which can sustain such a large increase. At coronal temperatures below 5 MK radiative losses dominate conductive losses, as seen also in solar coronal observations, however the magnitude by which radiative losses exceed conductive losses is a maximum of 10^{6} at 2.5 MK. At temperatures above 5 MK however conductive losses dominate, and by a large amount.

9. Conclusions

Through high quality spectroscopic observations and extensive wavelength coverage, we are able to determine a number of properties of the quiescent atmosphere of the dMe flare star EV Lac.

Nonthermal broadening in transition region line profiles appears to peak at temperatures $\leq 10^5$K, in contrast with the Sun. This behavior is also manifested in another active dMe star, AD Leo. Further investigation is needed to determine if this is a characteristic of most active stars; the enhancement due to turbulent pressure support in the transition region has implications for structure and dynamics.

We are able to constrain electron densities across two orders of magnitude in the transition region and corona, detailing a nearly constant pressure in the transition region and low temperature corona. The high temperature coronal material appears to be characterized by a large jump in pressure. Based on modeling the observed $P(T_e)$ from the emission measure distribution, we find no evidence to support a corona in hydrostatic equilibrium. Large magnetic field strengths are required to confine the high temperature coronal plasma. Coronal spectral analysis reveals a continuous distribution of temperatures and evidence for sub-Solar abundances. We extend the differential emission measure to transition region and upper chromospheric temperatures with the use of STIS and FUSE spectra; there is a deep emission measure minimum in the transition region. We cannot at this point determine whether an abundance gradient exists in EV Lac's outer atmosphere; we explored two possibilities, a coronal abundance pattern in the corona and solar photospheric abundances elsewhere, in addition to a coronal abundance pattern throughout EV Lac's upper atmosphere, and find little difference in the atmospheric properties.

Using low density ionization balance calculations reveals a discrepancy in Li- and Na-like ions in comparing flux predictions from the differential emission measure with observed fluxes. This may arise from ignoring the density dependence of dielectronic recombination rates in calculating ionization balance, or dynamical effects, or both. There is an urgent need to resolve this discrepancy, particularly for stellar studies, as these brightest transitions are used heavily in estimating the amount of material in transition region plasmas. The discrepancy can only be revealed when a suitably exposed spectrum contains diagnostic information at the same temperatures as these transitions, a situation which occurs only for a limited number of stars. Thus there is the potential for misinterpretation of the data if this effect is not resolved, and the pessimistic prospect for future UV spectroscopic missions means astronomers will be relying heavily on already obtained archival data.

Based on observed electron densities and emission measure distributions, the timescale for upper atmospheric material to lose energy is short, requiring significant continued heating. Calculations of analytic expressions for radiative and conductive loss rates show that a large amount of energy is being lost at high temperatures, which argues for an enhanced amount of energy input at the highest coronal temperatures. These implications rest to a large degree on the high electron pressures found in the corona from electron-density sensitive line ratios. The DEM shape is consistent with flare heating arguments, although statistical comparisons of flare and non-flare quantities requires a better defined knowledge of stellar flare physics than is revealed by current flare observations.

EV Lac is detected at a radio frequency of 15 GHz (2 cm) for the first time. This places constraints on the amount of gyroresonance emission, and rules out the high temperature thermal coronal plasma being spatially coincident with the radio emission source. By assuming that the bulk of cm-wavelength radio emission arises from accelerated electrons in a dipolar field configuration, we can constrain the field strengths and total number density of accelerated electrons for both a global dipole and one buried to a smaller depth. Generally equatorial surface field strengths $\leq$ a few hundred Gauss are required to explain the radio spectrum.

The constraints on electron pressure, timescales for loss, volumes and filling factors suggests a two-phase thermal corona: a low temperature corona occupied by a large volume of plasma, and a high temperature corona with small length scales. The radio-emitting corona also appears to be inhomogeneous, but have a large length scale. The relationship between high temperature coronal plasma and an origin in a flare heating process suggests a link with the radio emission source if accelerating electrons and heating coronal plasmas are a fundamental consequence of flares. However, the high frequency radio observations raise constraints on the spatial relationship between the high temperature coronal plasma and accelerated particles. More detailed models of coronal structure are needed to explain this hypothesis within the observational constraints discussed here.

This represents the results of VLA project AO160.

A. Appendix: Derivation of Analytic Expressions for Divergences of Conductive Losses

Here we derive the analytic expressions for the conductive flux. Using equation (6-9) for the radiative flux, the radiative loss rate is

$$\nabla \cdot F_r(T_e) = \frac{\phi(T_e)\psi(T_e)\Delta \log T}{4\pi R^2} \tag{A1}$$

Using equation (6-13) for the conductive flux, we calculate the divergence analytically as

$$\nabla \cdot F_c = \frac{(1 + \frac{F_{c,cl}}{F_{c,sat}})\frac{dF_{c,cl}}{ds} - F_{c,cl}\frac{d}{ds}(\frac{F_{c,cl}}{F_{c,sat}})}{(1 + \frac{F_{c,cl}}{F_{c,sat}})^2} \tag{A2}$$

where $dF_{c,cl}/ds$ is (using equation (6-11))

$$\frac{dF_{c,cl}}{ds} = -\kappa T^{3/2} \left(\frac{dT}{ds}\right)^2 \left[\frac{3}{2} + \frac{d\ln P}{d\ln T} + \frac{d\ln CEM}{d\ln T}\right] \tag{A3}$$

and

$$\frac{d}{ds}\left(\frac{F_{c,cl}}{F_{c,sat}}\right) = \frac{4\sqrt{m_e}\kappa}{k_B^{3/2}} \frac{T}{n_e} \frac{dT}{ds} \tag{A4}$$

REFERENCES

Ake, T. B., Dupree, A. K., Young, P. R., Linsky, J. L., Malina, R. F., Griffiths, N. W., Siegmund, O. H. W., & Woodgate, B. E. 2000, ApJ, 538, L87

Allred, J. C., Hawley, S. L., Abbett, W. P., & Carlsson, M. 2005, ApJ, 630, 573

—. 2006, ArXiv Astrophysics e-prints

Aschwanden, M. J., Nightingale, R. W., & Alexander, D. 2000, ApJ, 541, 1059

Ayres, T. R., Brown, A., Harper, G. M., Osten, R. A., Linsky, J. L., Wood, B. E., & Redfield, S. 2003, ApJ, 583, 963

Bowyer, S. & Malina, R. F. 1991, in Extreme Ultraviolet Astronomy, 397

Brickhouse, N. S., Raymond, J. C., & Smith, B. W. 1995, ApJS, 97, 551

Cook, J. W. & Nicolas, K. R. 1979, ApJ, 229, 1163

Cram, L. E. 1982, ApJ, 253, 768

Del Zanna, G., Landini, M., & Mason, H. E. 2002, A&A, 385, 968

Delfosse, X., Forveille, T., Perrier, C., & Mayor, M. 1998, A&A, 331, 581

Dere, K. P., Landi, E., Mason, H. E., Monsignori Fossi, B. C., & Young, P. R. 1997, A&AS, 125, 149

Dere, K. P. & Mason, H. E. 1993, Sol. Phys., 144, 217

Duflot, M., Figon, P., & Meyssonnier, N. 1995, A&AS, 114, 269

Dulk, G. A. 1985, ARA&A, 23, 169

Feldman, U. & Laming, J. M. 2000, Phys. Scr, 61, 222

Fisher, G. H., Canfield, R. C., & McClymont, A. N. 1985, ApJ, 289, 425

Güdel, M., Audard, M., Kashyap, V. L., Drake, J. J., & Guinan, E. F. 2003, ApJ, 582, 423

Gizis, J. E. 1997, AJ, 113, 806

Golub, L., Hartquist, T. W., & Quillen, A. C. 1989, Sol. Phys., 122, 245

Grevesse, N. & Sauval, A. J. 1998, Space Science Reviews, 85, 161

—. 1999, A&A, 347, 348

Griffiths, N. W. 1999, ApJ, 518, 873

Güdel, M. & Benz, A. O. 1989, A&A, 211, L5

Hünsch, M., Schmitt, J. H. M. M., Sterzik, M. F., & Voges, W. 1999, A&AS, 135, 319

Hawley, S. L., Allred, J. C., Johns-Krull, C. M., Fisher, G. H., Abbett, W. P., Alekseev, I., Avgoloupis, S. I., Deustua, S. E., Gunn, A., Seiradakis, J. H., Sirk, M. M., & Valenti, J. A. 2003, ApJ, 597, 535

Hempelmann, A., Schmitt, J. H. M. M., Schultz, M., Ruediger, G., & Stepien, K. 1995, A&A, 294, 515

Herczeg, G. J., Walter, F. M., Linsky, J. L., Gahm, G. F., Ardila, D. R., Brown, A., Johns-Krull, C. M., Simon, M., & Valenti, J. A. 2005, AJ, 129, 2777

Johns-Krull, C. M. & Valenti, J. A. 1996, ApJ, 459, L95

Jordan, C. 1991, in Mechanisms of Chromospheric and Coronal Heating, Proceeds of the International Conference, eds. P. Ulmschneider, E. R. Priest, R. Rosner (Berlin: Springer-Verlag), 300

Jordan, C. 1996, Ap&SS, 237, 13

Judge, P. G., Woods, T. N., Brekke, P., & Rottman, G. J. 1995, ApJ, 455, L85

Krucker, S. & Hudson, H. S. 2004, in ESA SP-575: SOHO 15 Coronal Heating, 247

Kruk, J., Murphy, E., & Young, P. 2001, The CalFUSE Pipeline Reference Guide, http://fuse.pha.jhu.edu/analysis/pipeline_reference.html (Baltimore: Johns Hopkins University)

Laming, J. M., Drake, J. J., & Widing, K. G. 1995, ApJ, 443, 416

Lenz, D. D., Deluca, E. E., Golub, L., Rosner, R., & Bookbinder, J. A. 1999, ApJ, 517, L155

Leto, G., Pagano, I., Linsky, J. L., Rodonò, M., & Umana, G. 2000, A&A, 359, 1035

Linsky, J. L. & Wood, B. E. 1994, ApJ, 430, 342

Mazzotta, P., Mazzitelli, G., Colafrancesco, S., & Vittorio, N. 1998, A&AS, 133, 403

Mitra-Kraev, U., Harra, L. K., Güdel, M., Audard, M., Branduardi-Raymont, G., Kay, H. R. M., Mewe, R., Raassen, A. J. J., & van Driel-Gesztelyi, L. 2005, A&A, 431, 679

Moos, H. W., Cash, W. C., Cowie, L. L., Davidsen, A. F., Dupree, A. K., Feldman, P. D., Friedman, S. D., Green, J. C., Green, R. F., Gry, C., Hutchings, J. B., Jenkins, E. B., Linsky, J. L., Malina, R. F., Michalitsianos, A. G., Savage, B. D., Shull, J. M., Siegmund, O. H. W., Snow, T. P., Sonneborn, G., Vidal-Madjar, A., Willis, A. J., Woodgate, B. E., York, D. G., Ake, T. B., Andersson, B.-G., Andrews, J. P., Barkhouser, R. H., Bianchi, L., Blair, W. P., Brownsberger, K. R., Cha, A. N., Chayer, P., Conard, S. J., Fullerton, A. W., Gaines, G. A., Grange, R., Gummin, M. A., Hebrard, G., Kriss, G. A., Kruk, J. W., Mark, D., McCarthy, D. K., Morbey, C. L., Murowinski, R., Murphy, E. M., Oegerle, W. R., Ohl, R. G., Oliveira, C., Osterman, S. N., Sahnow, D. J., Saisse, M., Sembach, K. R., Weaver, H. A., Welsh, B. Y., Wilkinson, E., & Zheng, W. 2000, ApJ, 538, L1

Morrison, R. & McCammon, D. 1983, ApJ, 270, 119

Ness, J.-U., Güdel, M., Schmitt, J. H. M. M., Audard, M., & Telleschi, A. 2004, A&A, 427, 667

Neupert, W. M., Newmark, J., Delaboudinière, J.-P., Thompson, B. J., Catura, R. C., Moses, J. D., Gurman, J. B., Portier-Fozzani, F., Gabriel, A. H., Artzner, G., Clette, F., Cugnon, P., Maucherat, A. J., Defise, J. M., Jamar, C., Rochus, P., Dere, K. P., Howard, R. A., Michels, D. J., Freeland, S., Lemen, J. R., & Stern, R. A. 1998, Sol. Phys., 183, 305

Osten, R. A., Ayres, T. R., Brown, A., Linsky, J. L., & Krishnamurthi, A. 2003, ApJ, 582, 1073

Osten, R. A., Hawley, S. L., Allred, J. C., Johns-Krull, C. M., & Roark, C. 2005, ApJ, 621, 398

Parker, E. N. 1988, ApJ, 330, 474

Pestalozzi, M. R., Benz, A. O., Conway, J. E., & Güdel, M. 2000, A&A, 353, 569

Porquet, D., Mewe, R., Dubau, J., Raassen, A. J. J., & Kaastra, J. S. 2001, A&A, 376, 1113

Priest, E. R., Foley, C. R., Heyvaerts, J., Arber, T. D., Mackay, D., Culhane, J. L., & Acton, L. W. 2000, ApJ, 539, 1002

Reale, F. & Peres, G. 2000, ApJ, 528, L45

Redfield, S., Linsky, J. L., Ake, T. B., Ayres, T. R., Dupree, A. K., Robinson, R. D., Wood, B. E., & Young, P. R. 2002, ApJ, 581, 626

Reid, I. N., Hawley, S. L., & Gizis, J. E. 1995, AJ, 110, 1838

Robrade, J. & Schmitt, J. H. M. M. 2005, A&A, in press

Rosner, R., Tucker, W. H., & Vaiana, G. S. 1978, ApJ, 220, 643

Saar, S. H. 1994, in IAU Colloquium 143 Poster Session: The Sun as a Variable Star: Solar and Stellar Irradiance Variations, eds. J.M. Pap, C. Frolich, H.S. Hudson, and S. Solanki, (Cambridge: Cambridge Univ. Press), 147–158

Sahnow, D. J., Moos, H. W., Friedman, S. D., Blair, W. P., Conard, S. J., Kruk, J. W., Murphy, E. M., Oegerle, W. R., & Ake, T. B. 2000, in Proc. SPIE Vol. 4139, p. 131-136, Instrumentation for UV/EUV Astronomy and Solar Missions, Silvano Fineschi; Clarence M. Korendyke; Oswald H. Siegmund; Bruce E. Woodgate; Eds., 131–136

Sciortino, S., Maggio, A., Favata, F., & Orlando, S. 1999, A&A, 342, 502

Sim, S. A. & Jordan, C. 2005, MNRAS, 361, 1102

Smith, D. F. & Auer, L. H. 1980, ApJ, 238, 1126

Smith, R. K., Brickhouse, N. S., Liedahl, D. A., & Raymond, J. C. 2001, ApJ, 556, L91

Spitzer, L. 1962, Physics of Fully Ionized Gases (Physics of Fully Ionized Gases, New York: Interscience (2nd edition), 1962)

Testa, P., Drake, J. J., & Peres, G. 2004, ApJ, 617, 508

Valenti, J. A., Johns-Krull, C. M., & Piskunov, N. 1998, in ASP Conf. Ser. 154: Cool Stars, Stellar Systems, and the Sun, 1357

van den Oord, G. H. J., Mewe, R., & Brinkman, A. C. 1988, A&A, 205, 181

Vilhu, O. & Walter, F. M. 1987, ApJ, 321, 958

White, S. M., Kundu, M. R., & Jackson, P. D. 1989, A&A, 225, 112

White, S. M., Lim, J., & Kundu, M. R. 1994, ApJ, 422, 293

Wikstol, O., Judge, P. G., & Hansteen, V. 1998, ApJ, 501, 895

Wood, B. E., Harper, G. M., Linsky, J. L., & Dempsey, R. C. 1996, ApJ, 458, 761

Wood, B. E., Linsky, J. L., & Ayres, T. R. 1997, ApJ, 478, 745

Wood, B. E., Müller, H.-R., Zank, G. P., Linsky, J. L., & Redfield, S. 2005a, ApJ, 628, L143

Wood, B. E., Redfield, S., Linsky, J. L., Müller, H.-R., & Zank, G. P. 2005b, ApJS, 159, 118

Young, P. R., Del Zanna, G., Landi, E., Dere, K. P., Mason, H. E., & Landini, M. 2003, ApJS, 144, 135

This preprint was prepared with the AAS LaTeX macros v5.2.

Table 1. VLA Multifrequency Observations

ν (MHz)	tos (s)	S_ν (mJy)	Beam Params (maj. x min., PA)[a]	V Flux (mJy)	Percent Pol (%)
4860	10570	0.51±0.04	5.2x3.5, 87	−0.11±0.02	−22.5±4
8460	10450	0.47±0.14	3.1x2.1, 89	−0.07±0.01	−16±2
14939	11940	0.34±0.04	7.7x5.5, 81	<0.11	...

[a] Beam major axis, beam minor axis in arcsec; PA=position angle in degrees

Table 2. Detected Lines in HST/STIS Spectrum

Transition	$\lambda_{\rm lab}$ (Å)	$\lambda_{\rm fit}$ (Å)	v (km s^{-1})	FHWM (km s^{-1})	flux (erg cm^{-2} s^{-1})	χ^2_ν	$\log T_{\rm eff}$ (K)
Single Gaussian Fits							
C III	1174.935	1174.935[1]	0	37.5±6.9	$5.33E{-}15\pm1.04E{-}15$	0.51	4.5
C III	1175.265	1175.265[1]	0	32.9±6.6	$4.53E{-}15\pm9.65E{-}16$	”	”
C III	1175.592	1175.592[1]	0	43.4±9.2	$6.54E{-}15\pm1.47E{-}15$	”	”
C III	1175.713	1175.713[1]	0	31.9±3.8	$1.07E{-}14\pm1.37E{-}15$	”	”
C III	1175.989	1175.989[1]	0	33.6±7.1	$4.58E{-}15\pm1.01E{-}15$	”	”
C III	1176.372	1176.372[1]	0	47.9±11.2	$4.79E{-}15\pm1.19E{-}15$	”	”
O V[2]	1218.390	1218.339	−11.0±1.5	30.0±3.2	$4.81E{-}15\pm5.21E{-}16$	0.54	5.4
N V	1242.804	1242.793	−1.1±0.7	33.3±1.7	$8.77E{-}15\pm4.56E$-16	0.59	5.3
Si II	1264.737	1264.723	−1.8±2.1	28.9±4.3	$1.32E{-}15\pm2.09E{-}16$	0.43	4.4
Si II	1265.001	1264.990	−1.1±3.6	30.6±7.4	$7.54E{-}16\pm1.88E{-}16$	”	4.4
Si III	1294.543	1294.534	−0.6±3.0	35.2 ±4.6	$1.28E{-}15\pm2.34E{-}16$	0.82	4.8
Si III	1296.726	1296.755	8.2±3.0	22.0±6.2	$5.20E{-}16\pm1.54E{-}16$	0.46	4.8
Si III[2,3]	1298.944	1298.925	−2.9±2.1	30.2±4.4	$1.32E{-}15\pm2.03E{-}16$	0.70	4.8
Si III	1303.323	1303.328	2.7±2.8	24.6±5.5	$5.75E{-}16\pm1.38E{-}16$	0.60	4.8
Si II	1309.274	1309.275	1.7±2.7	28.2±6.0	$8.20E{-}16\pm1.78E{-}16$	1.04	4.4
Fe XXI	1354.080	1354.072	−0.3±6.4	108.5±13.5	$3.27E{-}15\pm4.27E{-}16$	0.71	7.0
O V	1371.292	1371.296	2.4±1.7	23.6±3.5	$1.25E{-}15\pm1.91E{-}16$	0.66	5.4
O IV[2]	1401.171	1401.168	0.9±3.4	26.1±6.8	$5.89E{-}16\pm1.63E{-}16$	0.48	5.1
O IV	1399.779	1399.759	−2.8±6.0	26.1[4]	$3.19E{-}16\pm1.62E{-}16$	0.51	5.1
Si II	1526.706	1526.687	−2.4±2.8	26.7±5.7	$1.36E{-}15\pm3.07E{-}16$	0.49	4.4
Si II	1533.430	1533.410	−2.4±3.7	24.2±7.6	$1.70E{-}15\pm5.6E{-}16$	0.44	4.4
Double Gaussian Fits							
Si III	1206.499	1206.508	3.7±1.0	42.2±2.0	$1.71E{-}14\pm8.9E{-}16$	0.54	4.8
		1206.427	−16.4±10.0	130.2±21	$6.86E{-}15\pm1.14E{-}15$	”	”
N V	1238.821	1238.805	−2.4±0.5	29.8±1.0	$1.27E{-}14\pm4.86E{-}16$	0.82	5.3
		1238.816	0.3±2.2	77.7±4.8	$8.49E{-}15\pm5.47E{-}16$	”	”
Si IV	1393.755	1393.754	1.3±0.6	25.6±1.3	$9.18E{-}15\pm4.77E{-}16$	0.76	4.9
		1393.796	10.3±3.2	88.4±6.7	$7.52E{-}15\pm6.0E{-}16$	”	”
Si IV	1402.770	1402.766	0.6±0.6	23.9±1.2	$5.27E{-}15\pm2.89E{-}16$	0.97	4.9

Table 2—Continued

Transition	$\lambda_{\rm lab}$ (Å)	$\lambda_{\rm fit}$ (Å)	v (km s^{-1})	FHWM (km s^{-1})	flux (erg cm^{-2} s^{-1})	χ^2_ν	$\log T_{\rm eff}$ (K)
		1402.761	−0.4±3.8	63.7±8.0	3.17E−15±4.14E−16	”	”
C IV	1548.201	1548.200	1.3±0.5	31.8±1.0	4.30E−14±1.38E−15	0.89	5.0
		1548.217	4.6±4.3	135.9±9.0	2.08E−14±1.4E−15	”	”
C IV	1550.772	1550.758	−1.2±0.7	28.2±1.4	2.11E−14±1.1E−15	0.56	5.0
		1550.824	11.5±5.9	100.3±12.2	1.10E−14±1.4E−15	”	”

[1] Wavelengths of transitions fixed; width and peak flux allowed to vary.

[2] transition is sensitive to electron density

[3] feature is blended with another transition

[4] Width fixed to that of O IV λ1401.

[f] forbidden transition; not used in DEM analysis

[b] feature is blended with another transition of the same ion

Table 3. Expected and Observed Effectively Thin Line Ratios in STIS Spectrum

ion	Wavelengths	theo.	Obs.
Si II	1533.430/1526.706	2	1.25±0.5
C III	1175.265/1176.372	0.8	0.9±0.3
Si III	1296.726/1303.323	0.8	0.9±0.3
C III	1175.713/1174.935	3	2.0±0.5
Si IV	1393.755/1402.770	2	$1.7\pm0.1^{\mathrm{N}}$,$2.4\pm0.4^{\mathrm{B}}$
C IV	1548.201/1550.772	2	$2\pm0.1^{\mathrm{N}}$,$1.9\pm0.3^{\mathrm{B}}$
N V	1238.821/1242.804	2	$1.4\pm0.1^{\mathrm{N1}}$,2.4^{N2}

[N] Ratio value refers to flux ratio of the two narrow components.

[B] Ratio value refers to flux ratio of the two broad components.

[N1] Ratio value refers to flux ratio of narrow component of 1238 Å line to total flux of 1242 Å line.

[N2] Ratio value refers to flux ratio of narrow and broad components of 1238 Å line to total flux of 1242 Å line.

Table 4. Detected Lines in FUSE Spectra

λ_{lab} (Å)	Transition	λ_{fit} (Å)	flux 10^{-14} erg cm^{-2} s^{-1}	$\log T_{\mathrm{eff}}$
977.022	C III	...	7.9±1.1	4.9
1037.615	O VI	...	11.1±0.7	5.5
1031.914	O VI	...	22.9±1.1	5.5
974.860	Fe XVIII	...	0.53±0.31	6.8

Table 5. Detected Lines in EUVE Spectra

$\lambda_{\rm lab}$ (Å)	Transition	$\lambda_{\rm fit}$ (Å)	flux[a] (erg cm^{-2}s^{-1})	$\log T_{\rm eff}$
93.923	Fe XVIII	93.923±0.038	4.52E-14±9.90E-15	6.8
128.73	Fe XXI	128.730±0.045	3.67E-14±9.40E-15	7.0
132.85	Fe XXIII,Fe XX	132.85±0.032	6.90E-14±1.27E-14	
284.16	Fe XV	284.16±0.11	1.54E-13±3.13E-14	6.4
335.41	Fe XVI	335.41±0.10	1.57E-13±2.91E-14	6.4
360.761	Fe XVI	360.76±0.18	7.47E-14±2.65E-14	6.4

[a] Fluxes have been corrected for interstellar absorption, using N$_H$=4×10^{18} cm^{-2}.

Table 6. Detected Lines in Chandra Spectra

$\lambda_{\rm lab}$ (Å)	Transition	$\lambda_{\rm HEG}$ (Å)	$f_{\rm HEG}$[a] (erg cm^{-2} s^{-1})	$\lambda_{\rm MEG}$ (Å)	$f_{\rm MEG}$[a] (erg cm^{-2} s^{-1})	log $T_{\rm eff}$
6.1804	Si XIV	6.1821±0.0004	8.28E−14±5.99E−15	6.1808±0.0009	6.86E−14±5.81E−15	7.3
6.6479	Si XIII	6.6487±0.0005	8.84E−14±7.72E−15	6.6480±0.0007	8.87E−14±6.02E−15	6.9
6.6882	Si XIII	...	...	6.6854±0.0018	2.49E−14±4.35E−15	"
6.7403	Si XIII	6.7411±0.0004	6.38E−14±4.65E−15	6.7380±0.0010	5.23E−14±4.77E−15	"
8.4246	Mg XII	8.4204±0.0011	3.00E−14±5.91E−15	8.4203±0.0014	3.17E−14±4.18E−15	6.9
9.1687	Mg XI	9.1702±0.0007	3.15E−14±3.98E−15	9.1675±0.0012	3.59E−14±3.99E−15	6.9
9.2312	Mg XI	9.2306±0.0034	7.51E−15±4.70E−15	9.2305± 0.0034	9.62E−15±3.13E−15	"
9.3143	Mg XI	9.3156±0.0023	1.39E−14±5.75E−15	9.3131±0.0021	1.66E−14±3.29E−15	"
9.4797	Fe XXI	9.4782±0.0010	2.41E−14±4.21E−15	9.4776±0.0024	1.39E−14±3.13E−15	7.0
9.7085	Ne X	9.7097±0.0013	1.76E−14±4.08E-15	9.7096±0.0014	2.85E−14±3.72E−15	6.9
10.2385	Ne X	10.2399±0.0004	6.45E−14±4.82E−15	10.2382±0.0009	5.80E−14±4.78E−15	6.9
11.0010	Ne IX	...	...	10.9981±0.0027	1.82E−14±4.70E−15	6.7
11.1760	Fe XXIV	...	...	11.1777±0.0026[B]	1.71E−14±4.24E−15	7.3
11.7360	Fe XXIII	11.7375±0.0016	2.86E−14±8.31E−15	11.7363±0.0022	2.49E−14±5.12E−15	7.2
11.7700	Fe XXII	11.7685±0.0010	3.83E−14±7.27E−15	...	...	7.1
12.1375	Ne X	12.1350±0.0004	3.82E−13±2.65E−14	12.1314±0.0004	4.13E−13±1.39E−14	6.7
12.1610	Fe XXIII	12.1614±0.0009	3.93E−14±6.67E−15	...	...	7.1
12.2660	Fe XVII	...	...	12.2623±0.0020	3.33E−14±6.33E−15	6.7
12.2840	Fe XXI	12.2855±0.0012	3.42E−14±7.56E−15	12.2835±0.0017	4.21E−14±6.67E−15	7.0
13.4473	Ne IX	13.4480±0.0003	2.47E−13±1.34E−14	13.4459±0.0005	2.67E−13±1.37E−14	6.5
13.5180	Fe XIX	13.5185±0.0014	6.06E−14±1.52E−14	...	...	6.9

Table 6—Continued

$\lambda_{\rm lab}$ (Å)	Transition	$\lambda_{\rm HEG}$ (Å)	$f_{\rm HEG}$$^{\rm a}$ (erg cm^{-2} s^{-1})	$\lambda_{\rm MEG}$ (Å)	$f_{\rm MEG}$$^{\rm a}$ (erg cm^{-2} s^{-1})	log $T_{\rm eff}$
13.5531	Ne IX	13.5556±0.0022	3.44E−14±1.39E−14	13.5566±0.0027	3.05E−14±7.65E−15	6.5
13.6990	Ne IX	13.7005±0.0005	1.10E−13±1.07E−14	13.6971±0.0008	1.37E-13±1.04E-14	”
14.2080	Fe XVIII	14.2066±0.0008	9.60E−14±1.47E−14	14.2043±0.0013	8.71E−14±1.03E−14	6.9
14.3730	Fe XVIII	. . .	. . .	14.3719±0.0031	2.75E−14±8.00E−15	”
14.5340	Fe XVIII	. . .	. . .	14.5378±0.0033	2.35E−14±7.38E−15	”
15.0140	Fe XVII	15.0149±0.0003	2.51E−13±1.15E−14	15.0119±0.0007	2.83E−13±1.86E−14	6.7
15.1980	Fe XIX	. . .	. . .	15.1966±0.0033	3.26E−14±1.02E−14	6.9
15.2610	Fe XVII	15.2627±0.0017$^{\rm B}$	6.69E−14±2.05E−14	15.2607±0.0010$^{\rm B}$	1.06E−13±1.03E−14	6.7
15.4530	Fe XVII	. . .	. . .	15.4470±0.0028	2.31E−14±6.22E−15	6.7
15.6250	Fe XVIII	. . .	. . .	15.6244±0.0022	3.75E−14±7.89E−15	6.9
16.0710	Fe XVIII	. . .	. . .	16.0739±0.0015	6.84E−14±9.90E−15	”
16.7800	Fe XVII	. . .	. . .	16.7763±0.0009	1.54E−13±1.35E−14	6.7
17.0510	Fe XVII	. . .	. . .	17.0502±0.0008	2.37E−13±1.78E−14	”
17.0960	Fe XVII	. . .	. . .	17.0955±0.0009	2.01E−13±1.73E−14	”
18.9671	O VIII	. . .	. . .	18.9686±0.0005	9.29E−13±3.98E−14	6.4
21.6015	O VII	. . .	. . .	21.6031±0.0012	3.13E−13±3.58E−14	”
21.8036	O VII	. . .	. . .	21.8065±0.0026	1.01E−13±2.47E−14	”
22.0977	O VII	. . .	. . .	22.0977±0.0018	1.71E−13±2.84E−14	”
24.7792	N VII	. . .	. . .	24.7786±0.0029	7.49E−14±2.09E−14	”

[a] Fluxes have been corrected for interstellar absorption using $N_H=4\times10^{18}$ cm^{-2}.

[B] Blend

Table 7. Coronal Abundance Determinations

FIP (eV)	Element	Ions[a]	Value
14.534	N	VII	N/Fe=0.95±0.32
13.618	O	VII, VIII	O/Fe=0.80±0.04
21.564	Ne	IX,X	Ne/Fe=1.72±0.14
7.646	Mg	XI,XII	Mg/Fe=0.49±0.05
8.151	Si	XIII,XIV	Si/Fe=1.48±0.09
7.87	Fe	XV–XXIV	Fe/H=0.53±0.16

[a] Ionization stages used in coronal abundance determination

Table 8. Variability check: Fe XXI and Fe XVIII ratios

ratio	Observed[1]	Predicted[1]	$\mathrm{Log_{10}\ T_{max}} \pm 0.15$
— Fe XXI —			
$\lambda1354^{\mathrm{S}}/\lambda9.48^{\mathrm{C}}$	0.22±0.04	0.5–1.2	6.85–7.15
$\lambda1354^{\mathrm{S}}/\lambda12.284^{\mathrm{C}}$	0.11±0.02	0.08–0.15	6.85–7.15
$\lambda128.73^{\mathrm{E}}/\lambda9.48^{\mathrm{C}}$	1.93±0.56	5.–13.	6.85–7.15
$\lambda128.73^{\mathrm{E}}/\lambda12.284^{\mathrm{C}}$	0.96±0.28	0.8–1.6	6.85–7.15
$\lambda1354^{\mathrm{S}}/\lambda128.73^{\mathrm{E}}$	0.12±0.03	0.09–0.10	6.85–7.15
— Fe XVIII —			
$\lambda974^{\mathrm{F}}/\lambda14.208^{\mathrm{C}}$	0.06±0.04	0.04–0.12	6.65–7.05
$\lambda974^{\mathrm{F}}/\lambda16.07^{\mathrm{C}}$	0.08±0.05	0.14–0.30	6.65–7.05
$\lambda93.92^{\mathrm{E}}/\lambda14.208^{\mathrm{C}}$	0.49±0.12	0.32–1.05	6.65–7.05
$\lambda93.92^{\mathrm{E}}/\lambda16.07^{\mathrm{C}}$	0.66±0.17	1.2–2.8	6.65–7.05
$\lambda974^{\mathrm{F}}/\lambda93.92^{\mathrm{E}}$	0.12±0.07	0.109-0.118	6.65–7.05

[1] Energy flux ratios

[S] HST/STIS observation 2001 September

[F] FUSE observation 2002 July

[E] EUVE observation 1993 September

[C] Chandra observation 2001 September

Table 9. Densities Derived from UV and X-ray Line Ratios

Ion	ratio	R=f_1/f_2[1]	$\log_{10} T_0$	n_e (cm^{-3})
O IV	$\lambda 1401/\lambda 1399$	2.2±0.9	5.2 (T_{max})	$<1.6\times10^{11}$
O V	$\lambda 1218/\lambda 1371$	4.6±0.7	5.4 (T_{max})	1.0×10^{11} (7.4×10^{10}–1.6×10^{11}
O VII	$\lambda 22.10/\lambda 21.80$	2.0±1.0	6.4	3.0×10^{10}(8.7×10^{9}–9.5×10^{10}
Ne IX	$\lambda 13.70/\lambda 13.55$	3.6±0.9	6.7	$<1.7\times10^{11}$
Mg XI	$\lambda 9.31/\lambda 9.23$	1.4±0.6	6.9	1.0×10^{13} (4.3×10^{12}–2.6×10^{13})
Si XIII	$\lambda 6.74/\lambda 6.69$	2.1±0.4	6.9	$<1.8\times10^{13}$
Fe XVII	$\lambda 17.051/\lambda 17.096$	1.18±0.13	7.0	$< 10^{13}$

[1] Energy flux ratio

Table 10. Using the narrow line profile component in DEM analyses

Transition	f_{obs}/f_{pred}[a]	f_{obs}/f_{pred}[b]
Coronal Abundance Pattern		
N V λ1238	3.2	5.3
Si III λ1206	0.3	0.4
Si IV λ1393	0.7	1.3
Si IV λ1402	0.8	1.3
C IV λ1548	2.1	3.1
C IV λ1550	2.1	3.1
Hybrid Abundance Pattern		
N V λ1238	2.2	3.6
Si III λ1206	0.4	0.5
Si IV λ1393	1.5	2.8
Si IV λ1402	1.7	2.8
C IV λ1548	1.5	2.3
C IV λ1550	1.5	2.3

[a] Agreement between observed and predicted flux using integrated line flux of narrow Gaussian component

[b] Agreement between observed and predicted flux using integrated line flux of both Gaussian components

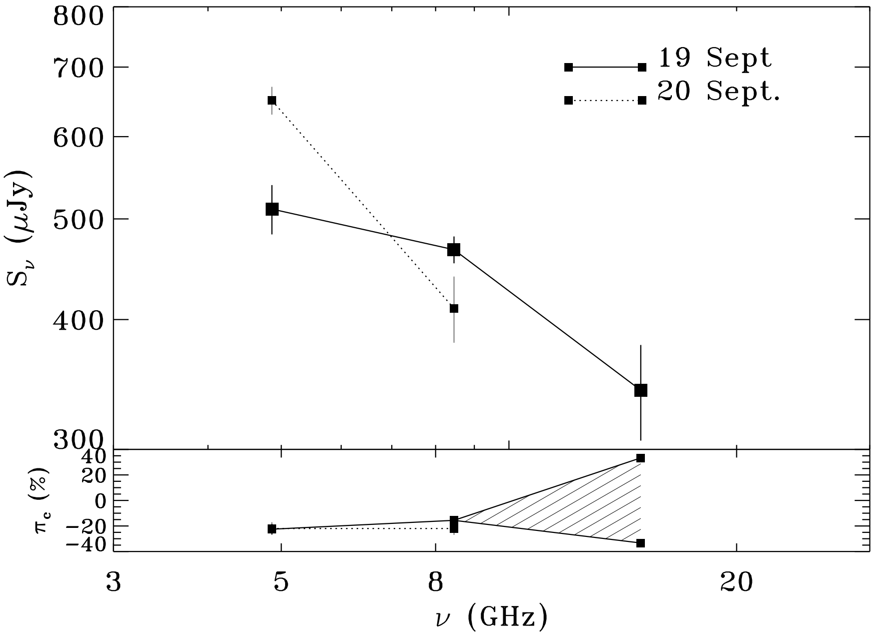

Fig. 1.— Observed radio flux densities of EV Lac on two consecutive days in 2001 September. Bottom panel shows the circular polarization spectrum.

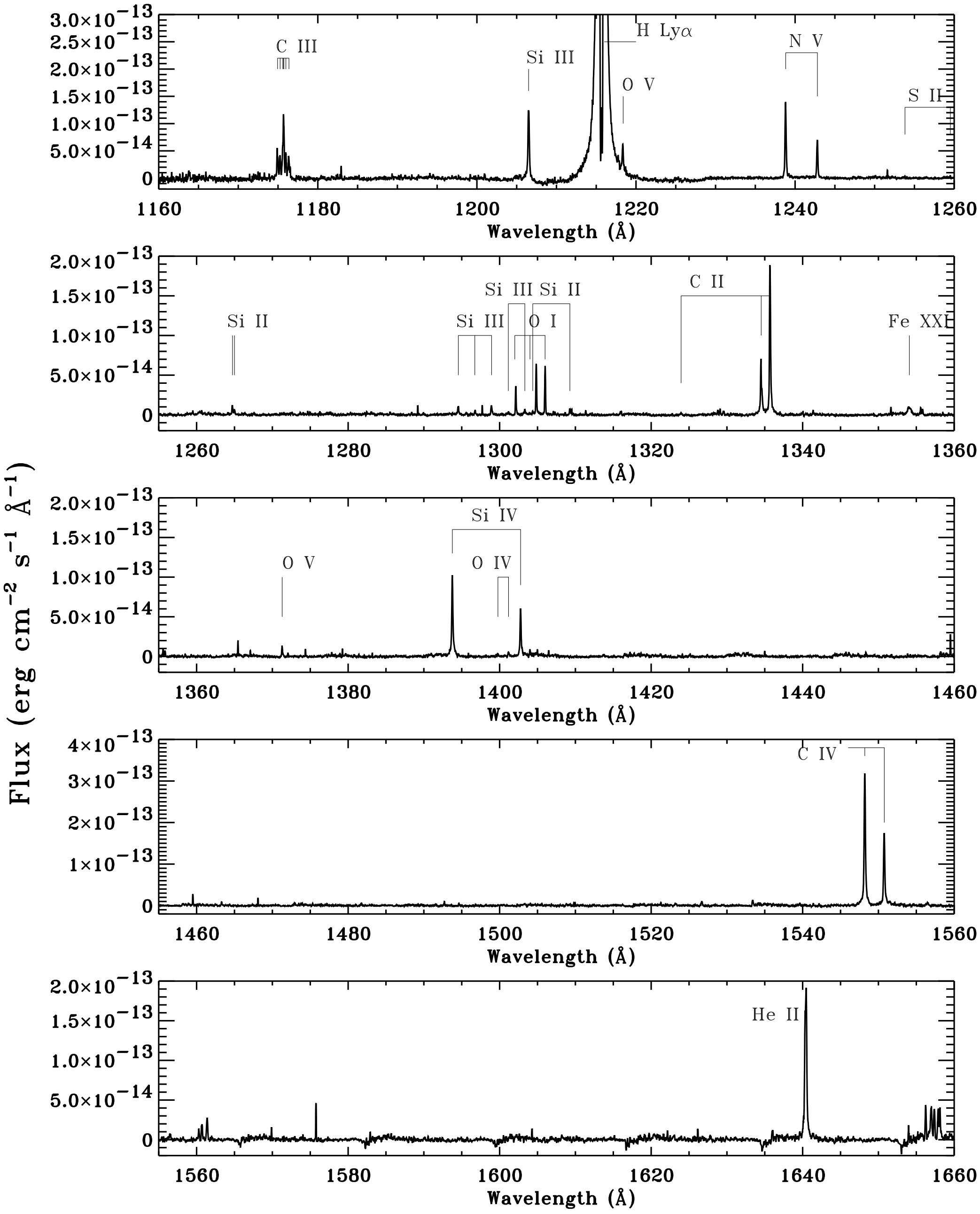

Fig. 2.— HST/STIS spectrum of EV Lac. Spectrum has been smoothed over 4 wavelength bins for clarity. Bright emission lines and those used in the DEM/density analyses are identified.

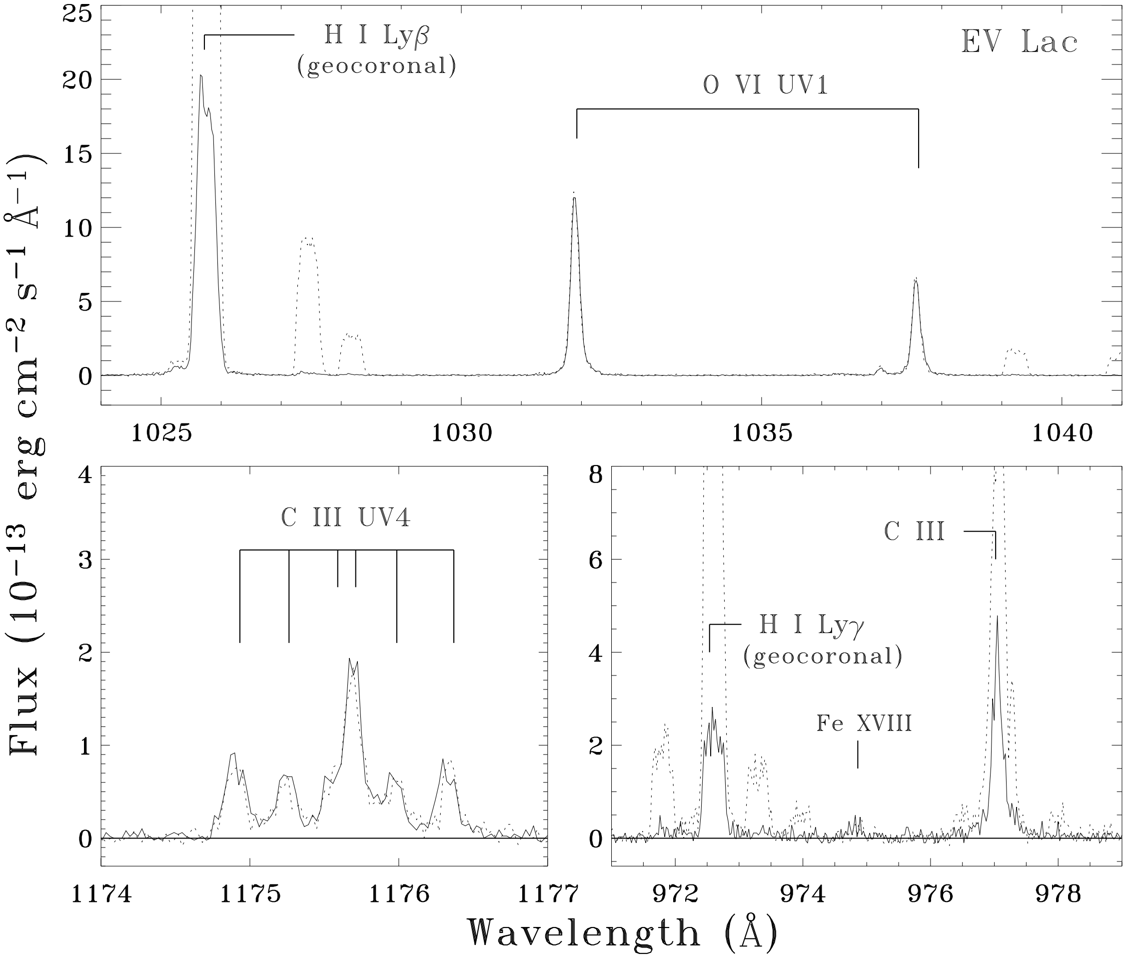

Fig. 3.— FUSE spectrum of EV Lac.

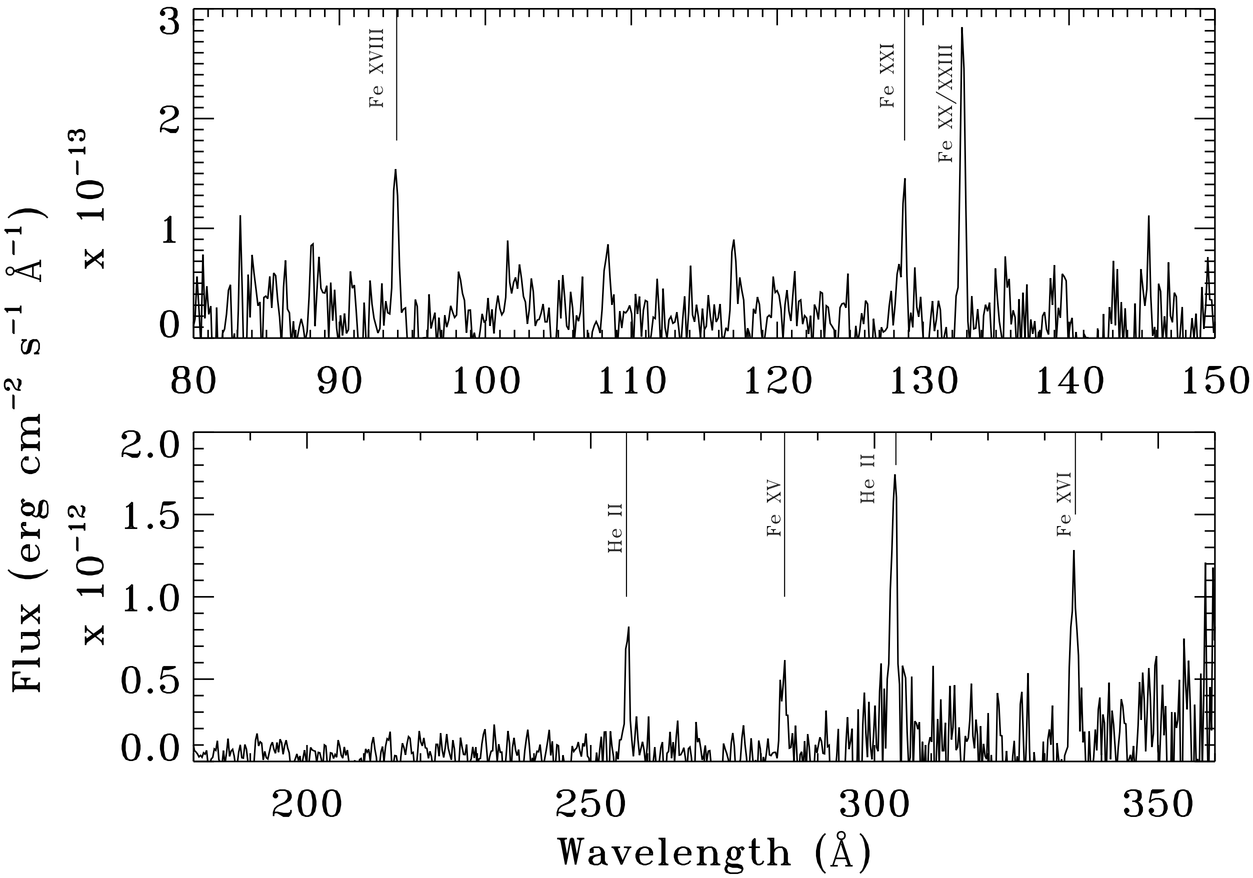

Fig. 4.— EUVE spectrum of EV Lac.

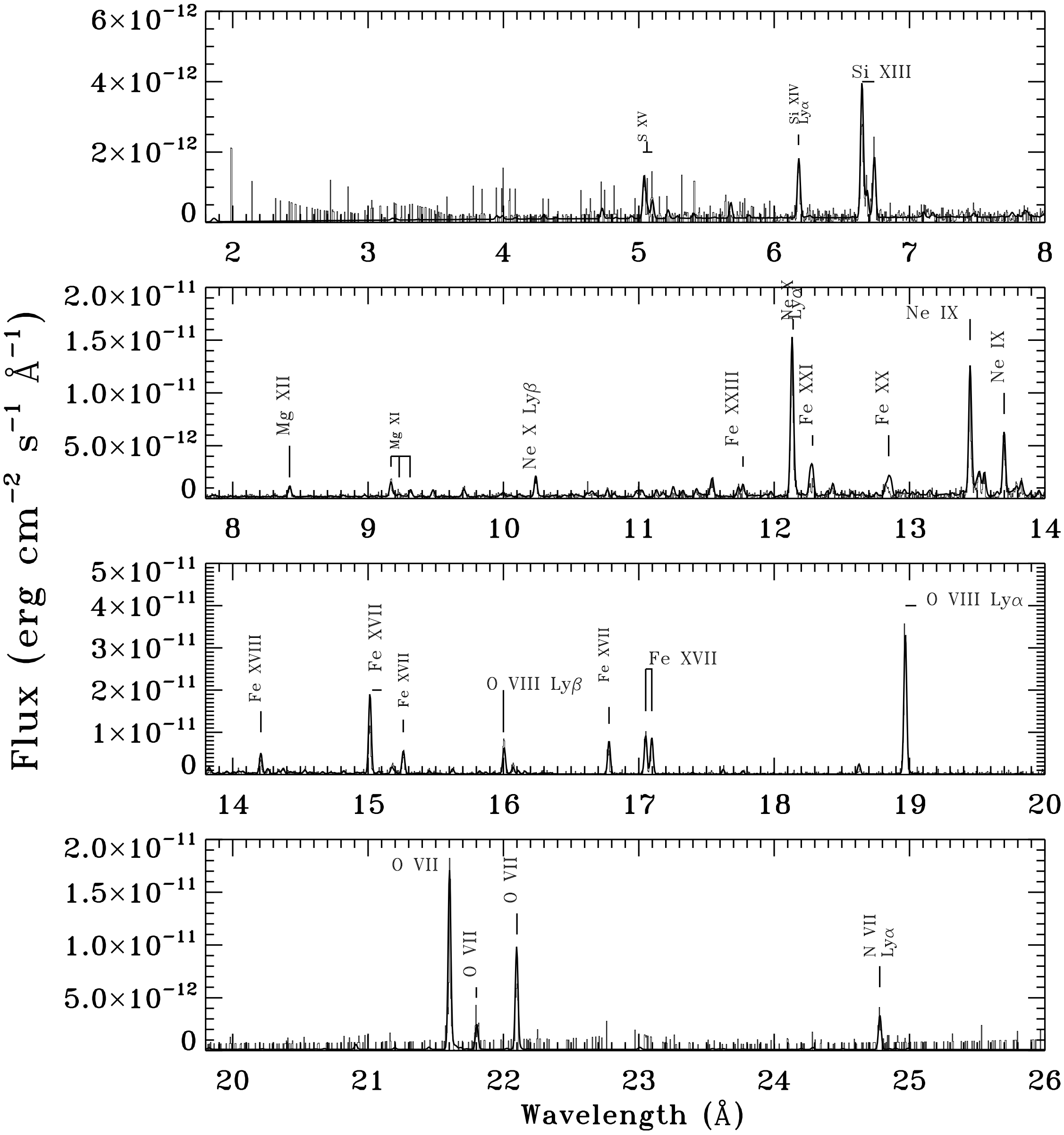

Fig. 5.— Chandra MEG spectrum of EV Lac (black histogram), with synthesized spectrum from DEM and abundance analysis in §5. Bright emission lines are identified.

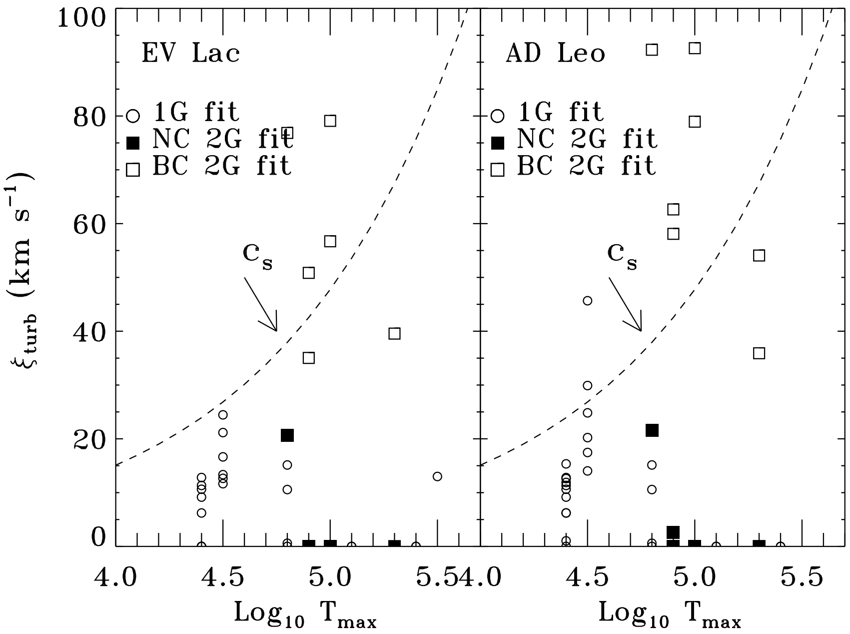

Fig. 6.— Nonthermal velocities deduced from excess broadening in line profiles found in STIS spectrum. “1G fit” refers to line profiles fit by a single Gaussian, “NC 2G fit” refers to the narrow component of a two Gaussian line profile fit, and “BC 2G fit” refers to the broad component of a two Gaussian line profile fit. The dashed line represents the sound speed of a fully ionized plasma assuming solar abundances. *(Left panel)* Trends for EV Lac; *(right panel)* trends for AD Leo.

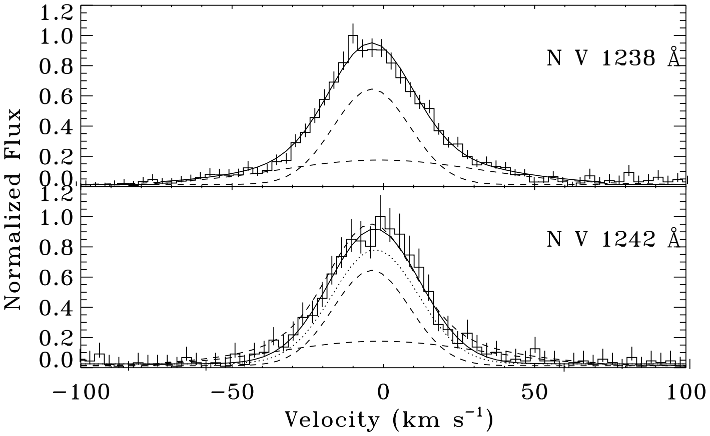

Fig. 7.— Comparison of λ1238 and λ1242 Å transitions of N V. The Gaussian line profiles are shown (dotted lines), as well as the result after convolving with the line spread function (solid line). The λ1238 line has higher S/N, being a factor of 2 brighter, and shows evidence for a broad second Gaussian. For comparison we overplot the single Gaussian fit from the λ1242 line to illustrate the excess flux in the wings of this profile.

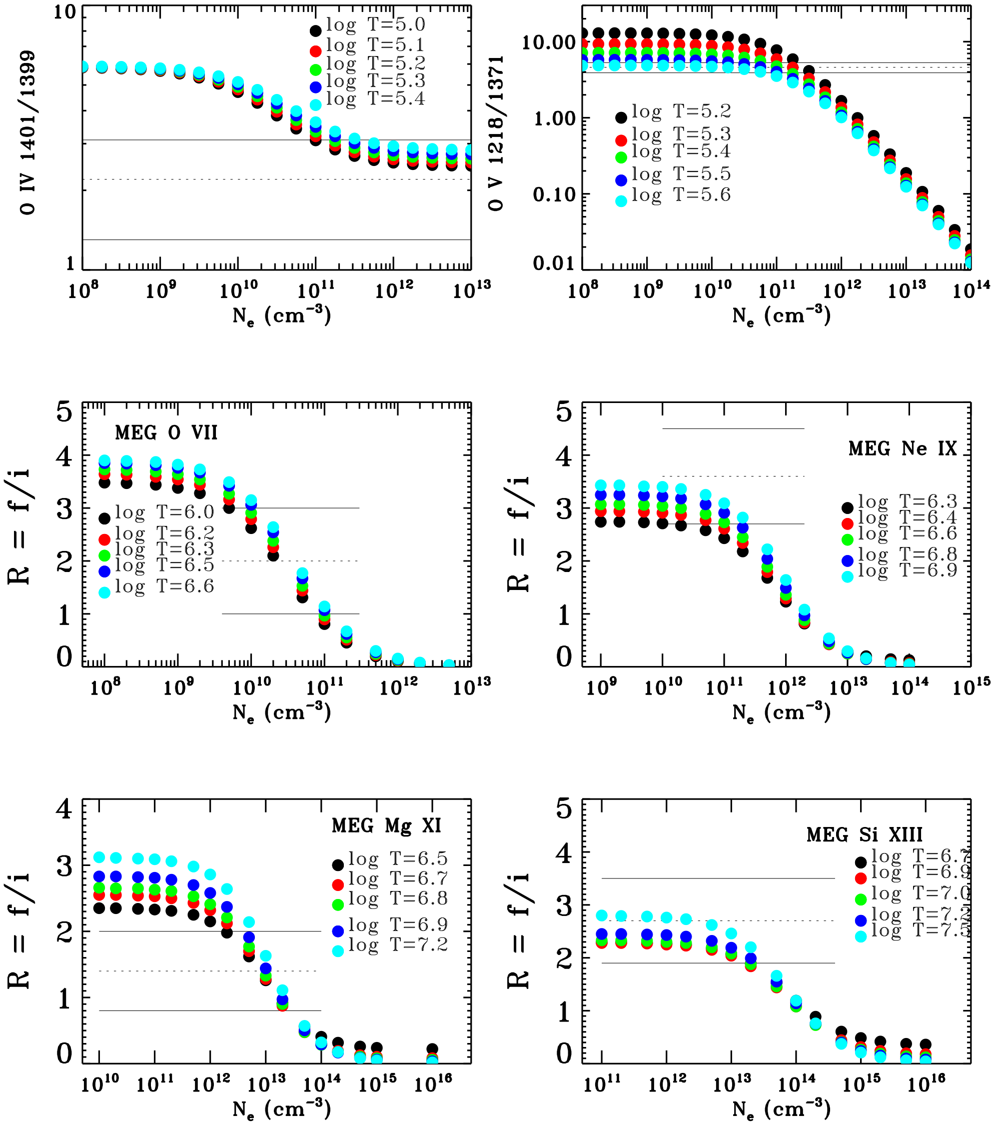

Fig. 8.— Electron densities in the transition region and corona of EV Lac, determined from line ratios of Chandra HEG/MEG and HST/STIS emission lines. Theoretical curves for Si XIII, Mg XI, Ne IX, and O VII are taken from Porquet et al. (2001); theoretical curves for O V and O IV are from CHIANTI v4.2 (Dere et al. 1997; Young et al. 2003).

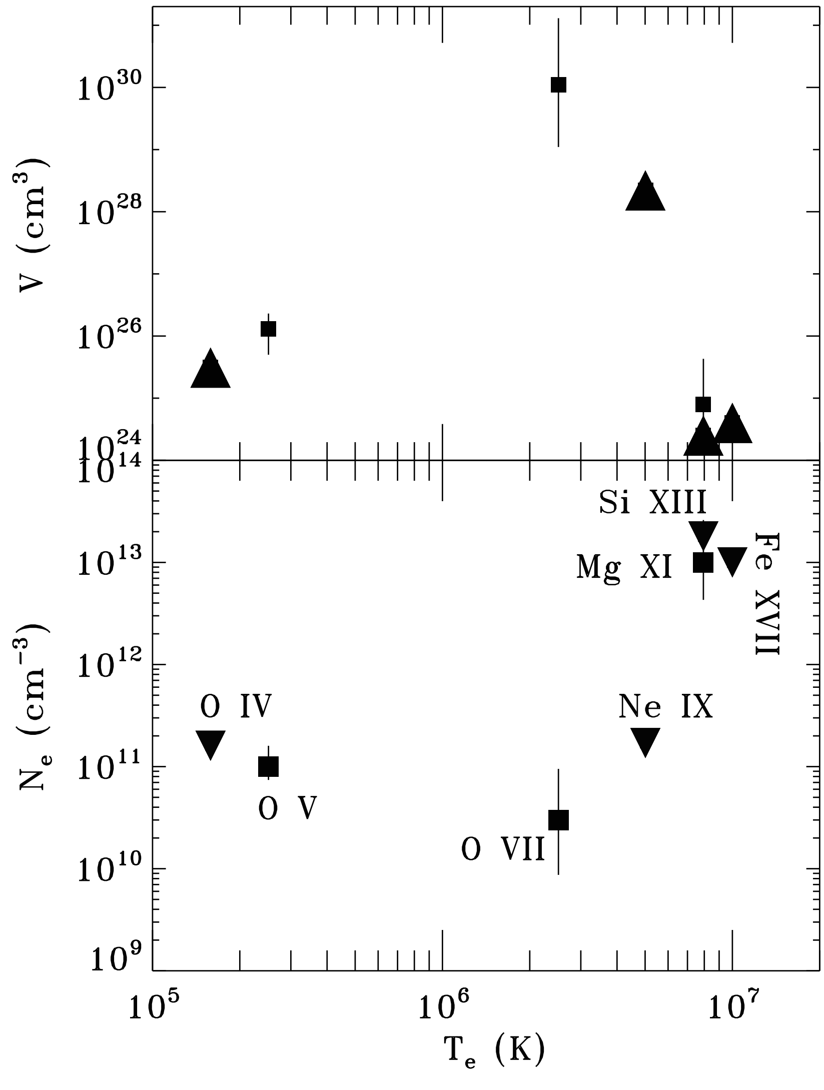

Fig. 9.— *(lower)* Dependence of electron density on electron temperature, using density diagnostics shown in Figure 8. *(upper)* Volume of plasma contributing to emission in the transition region and corona, using electron density estimates and emission measures.

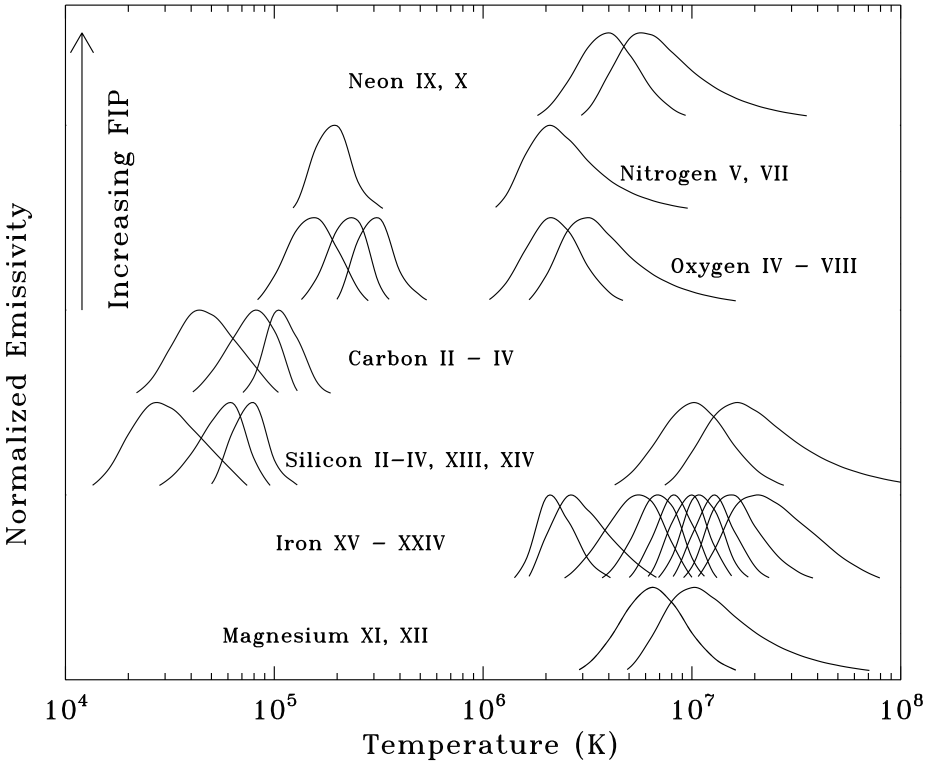

Fig. 10.— Temperature coverage of emission lines detected in STIS, FUSE, EUVE, and HETGS spectra. Elements are ordered in increasing First Ionization Potential (FIP). Individual emissivities have been normalized to illustrate their temperature coverage.

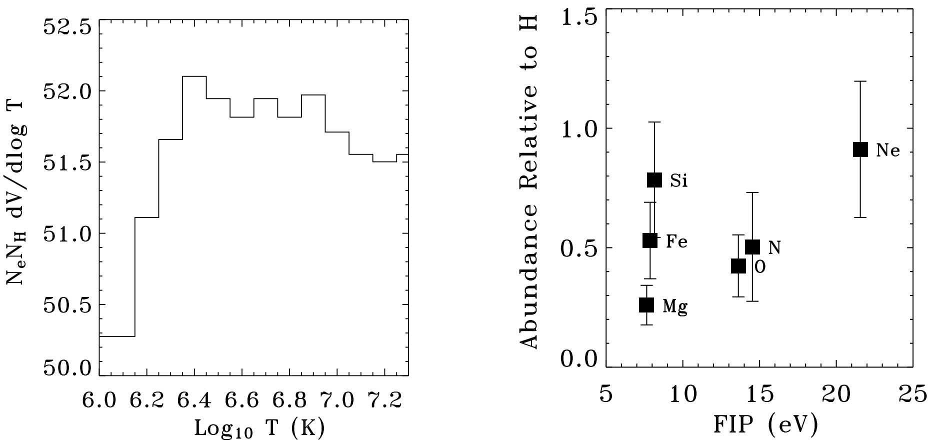

Fig. 11.— *(left)* Differential emission measure (DEM) distribution derived from the EUVE and Chandra spectra. *(right)* Abundances derived from Chandra spectra.

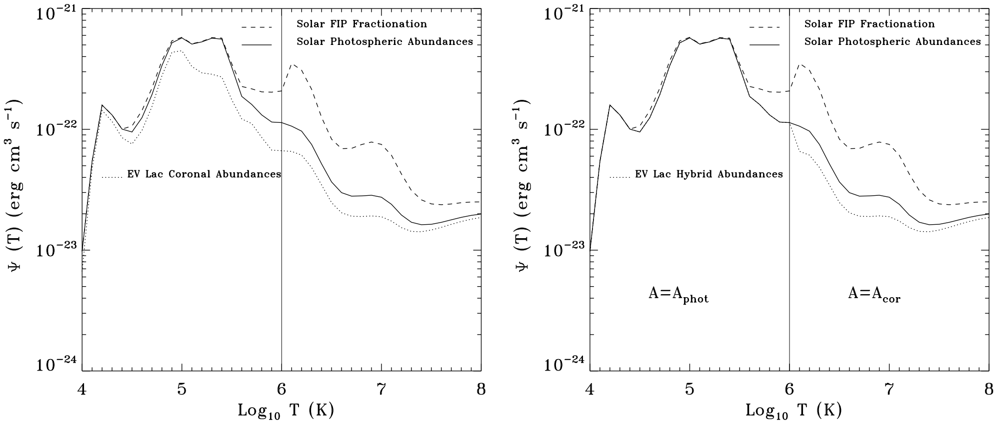

Fig. 12.— *(left)* Radiative loss function computed using atomic database from APEC v.1.3.1, with EV Lac's coronal abundance used at all temperatures. *(right)* Radiative loss function computed with a hybrid abundance pattern, consisting of EV Lac's coronal abundance at temperatures >1MK, and the solar photospheric abundances at lower temperatures. Insets to both figures illustrate the stellar coronal abundance pattern with FIP.

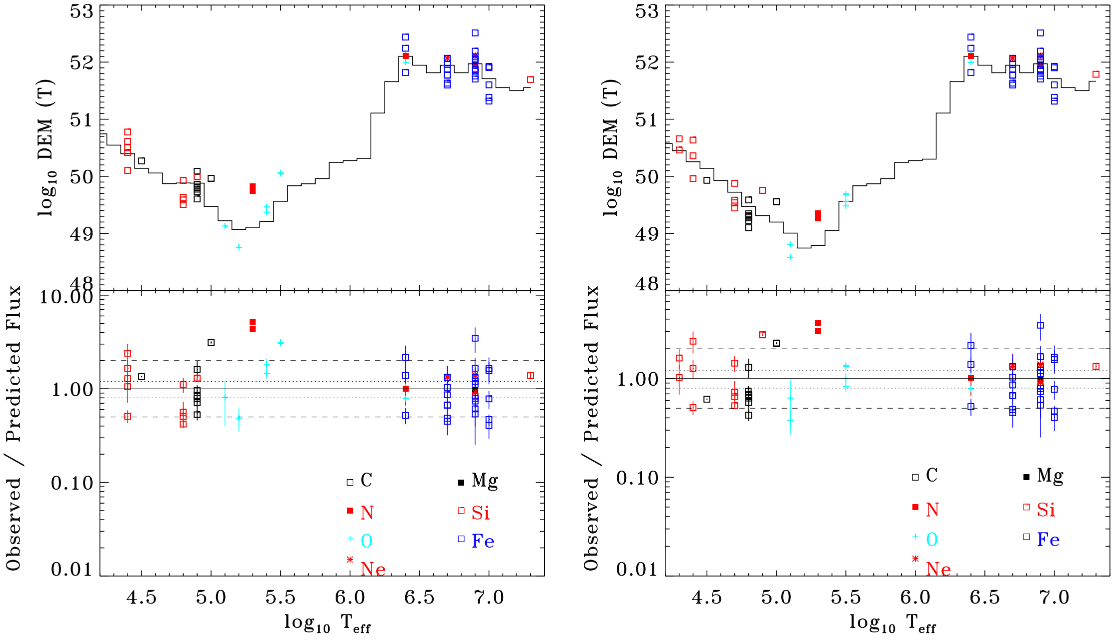

Fig. 13.— *(top left)* DEM reconstructed from STIS, FUSE, EUVE, and Chandra spectra using abundances derived from coronal spectra. Each point represents the transitions used in the DEM analysis: the points are plotted at the effective temperature, and the ordinate is the DEM at that temperature, multiplied by $f_{\rm obs}/f_{\rm pred}$. Legend is in the lower panel. *(bottom left)* Agreement between observed and predicted fluxes, plotted against effective temperature. Legend indicates which elements are being plotted. *(top right)* DEM reconstructed from STIS, FUSE, EUVE, and Chandra spectra using a hybrid abundance: coronal abundance pattern at T>1MK, and solar photospheric for T<1MK. Symbols and legend are as in top left. *(bottom right)* Same as bottom left, for the hybrid abundance case.

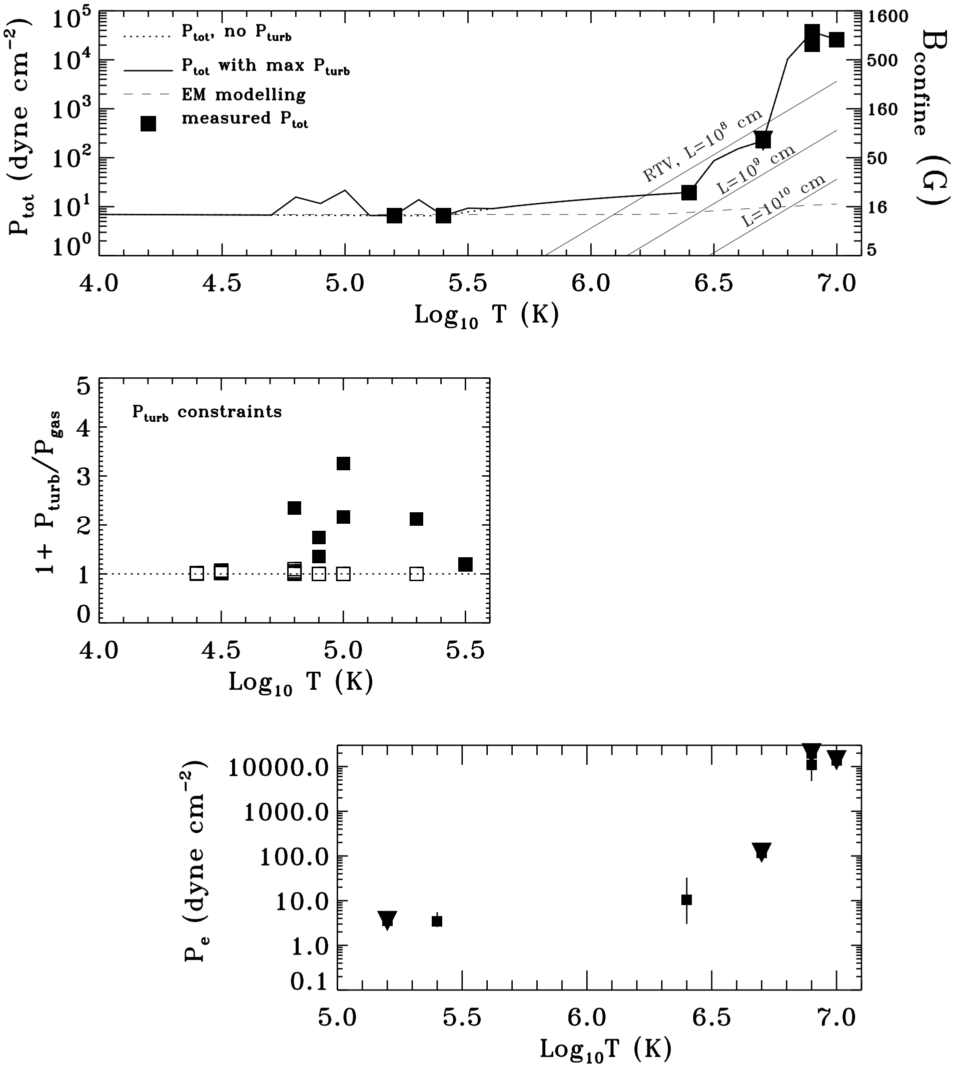

Fig. 14.— *(bottom)* Electron pressure constraints versus temperature, for the densities determined emission line ratios in §4. *(middle)*Calculation of enhancement over gas pressure afforded by turbulent pressure, deduced from the broadening of line profiles in the STIS spectrum. Circles refer to single Gaussian fits to line profiles; open squares refer to the narrow component of line profiles fit by two Gaussians; and filled squares refer to the broad components of such line profiles. *(top)* Total pressure versus temperature, using electron density constraints from line ratios and turbulent pressure calculations.

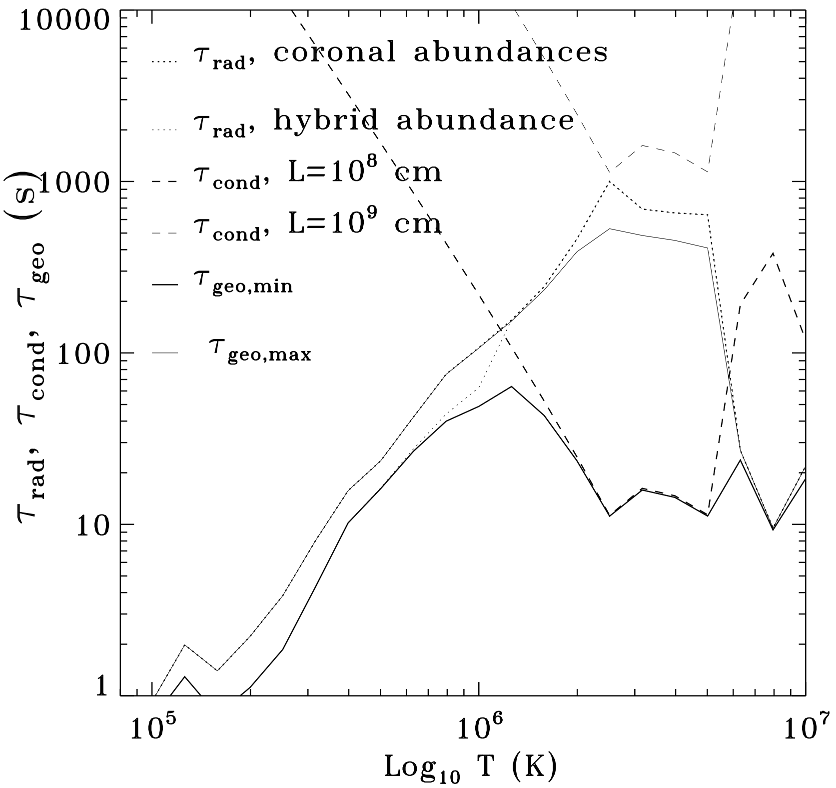

Fig. 15.— Timescales for radiative and conductive losses, calculated using the run of electron density with temperature shown in Figure 9, and the radiative loss functions shown in Figure 12. Conductive loss timescales are estimated using loop lengths of 10^8 and 10^9 cm, respectively.

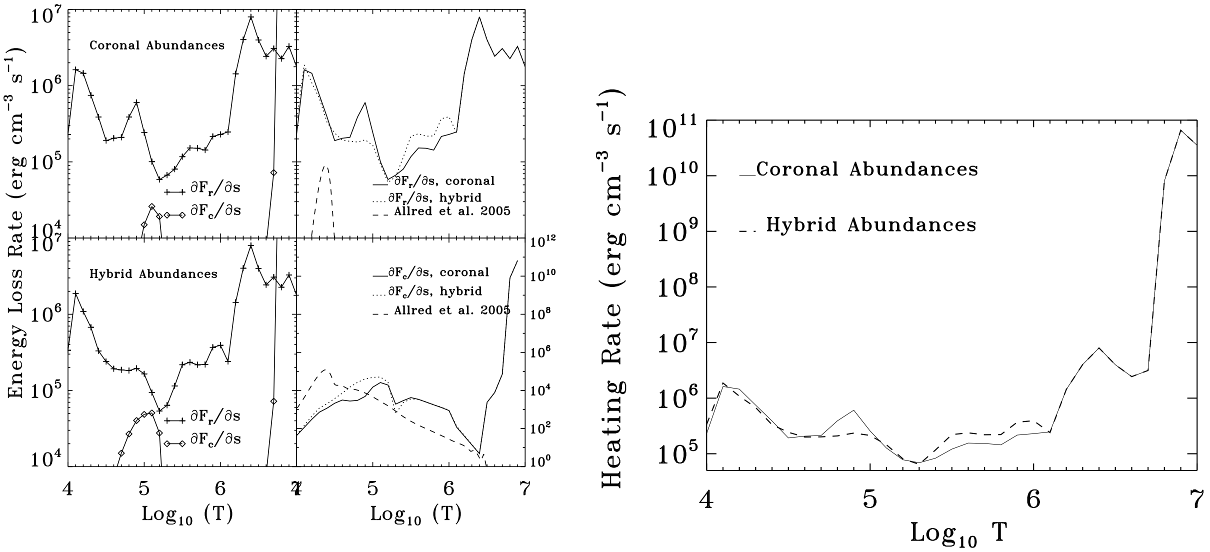

Fig. 16.— *(left)* Radiative and conductive losses estimated using the two DEMs, run of electron pressure with temperature, and radiative loss functions. The left-hand panels compare radiative and conductive losses for each abundance scenario; right-hand panels compare radiative and conductive losses with preflare model calculations of Allred et al. (2005) in the upper and lower panels, respectively. The large jump in conductive losses at $\log T = 6.4$ is due to the large inferred electron densities, and hence electron pressures, in the corona. See §6.3 for discussion. *(right)* Estimation of volumetric heating rate at each temperature in the atmosphere, by combining the conductive and radiative loss rates under the assumption of energy balance. The enhancement in the low temperature corona is due to large radiative loss rates, while the sharp spike in the high temperature corona is due to a precipitous jump in conductive loss rates.

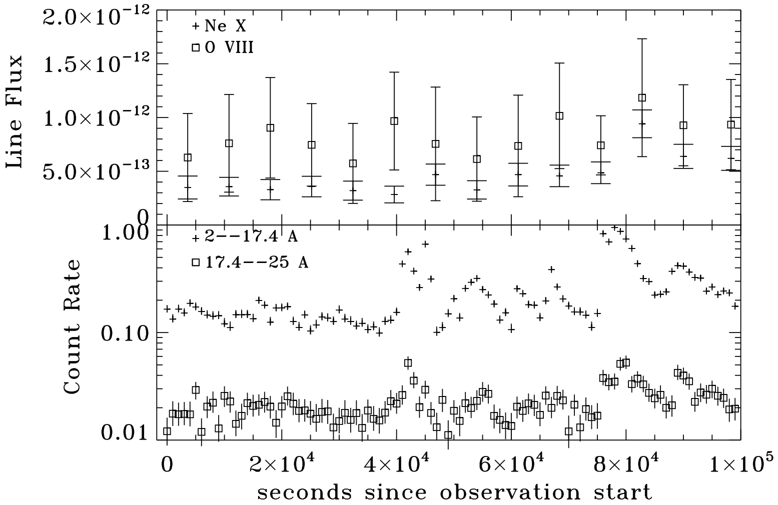

Fig. 17.— *(top)* Time variation of two strong lines during the Chandra observation — Ne X is formed at $\log T_{\rm eff}$ =6.7 and O VIII is formed at $\log T_{\rm eff}$= 6.4. Spectra were extracted in two hour time bins. Despite the large flares seen in the integrated light curve, there is no evidence for the high temperature line being more variable than the low temperature line. *(bottom)* Light curve of soft ($17.4< \lambda <25$ Å) and hard ($2< \lambda <17.4$ Å) photons in 1000 s bins during the Chandra observation. Enhancements are more noticeable in the hard light curve during large-scale flares, but there is no evidence for more variability in the hard light curve outside of large-scale flares.

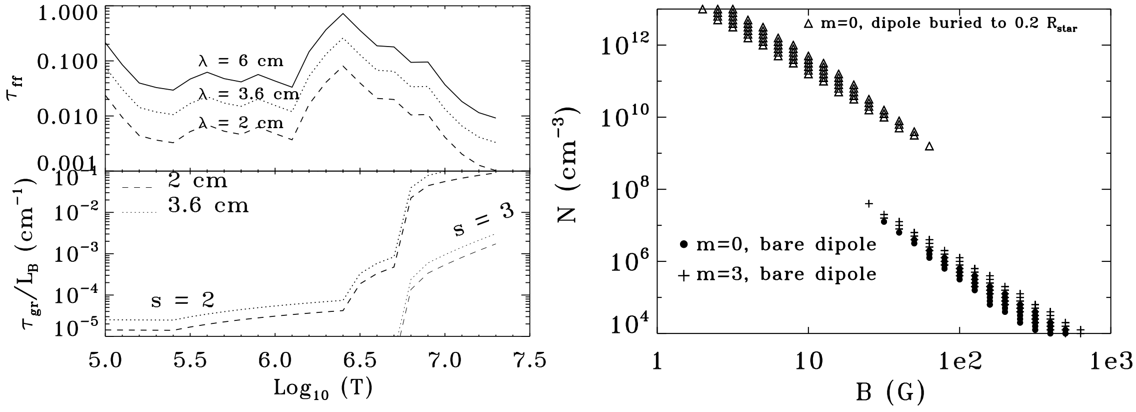

Fig. 18.— *(left)* Estimate of optical depths due to free-free (top) and gyroresonance (bottom) emission in the upper atmosphere of EV Lac. Gyroresonant optical depths are computed at two harmonics for each of the two highest frequencies detailed in our observations, relative to the unknown magnetic length scale. *(right)* Range of total nonthermal electron density and base magnetic field strength allowed in simple dipole models for the magnetic field geometry to reproduce the observed 15 GHz flux density (to within a factor of two) and spectral peak between 2 and 8 GHz. See §7 for more details.